

1 **Abiotic methane generation through reduction of serpentinite-hosted**  
2 **dolomite: implications for carbon mobility in subduction zones**

3 Weigang Peng<sup>a,b,c</sup>, Lifei Zhang<sup>a,\*</sup>, Simone Tumiati<sup>c</sup>,

4 Alberto Vitale Brovarone<sup>d,e</sup>, Han Hu<sup>a</sup>, Yachun Cai<sup>b</sup>, Tingting Shen<sup>f</sup>

5 <sup>a</sup> *MOE Key Laboratory of Orogenic Belts and Crustal Evolution, School of Earth*  
6 *and Space Sciences, Peking University, Beijing 100871, China*

7 <sup>b</sup> *Deep Sea Research Center, Pilot National Laboratory for Marine Science and*  
8 *Technology (Qingdao), Qingdao 266061, China*

9 <sup>c</sup> *Dipartimento di Scienze della Terra, Università degli Studi di Milano, via*  
10 *Mangiagalli 34, 20133 Milano, Italy*

11 <sup>d</sup> *Dipartimento di Scienze Biologiche, Geologiche e Ambientali, Alma Mater*  
12 *Studiorum Università di Bologna, Piazza di Porta San Donato 1, 40126 Bologna,*  
13 *Italy*

14 <sup>e</sup> *Sorbonne Université, Muséum National d'Histoire Naturelle, UMR CNRS 7590,*  
15 *IRD, Institut de Minéralogie, de Physique des Matériaux et de Cosmochimie,*  
16 *IMPMC, 4 Place Jussieu, 75005 Paris, France*

17 <sup>f</sup> *Institute of Geology, Chinese Academy of Geological Sciences, Beijing 100037,*  
18 *China*

19  
20 \*Corresponding author: Lifei Zhang

21 E-mail: lfzhang@pku.edu.cn

22 Telephone: +86-010-62751145

23 **ABSTRACT**

24 Abiotic methane has been increasingly detected at the surface of Earth and  
25 other terrestrial planets, exerting a strong effect on the study of  
26 chemolithoautotrophic life and thus astrobiology. In contrast, abiotic methane  
27 generation in subduction zones, which is intimately linked to questions such as  
28 the mechanisms of deep carbon mobility, has received scarce attention.  
29 Experiments elucidated the significant production of abiotic methane through  
30 reduction of carbonate minerals under subduction zone conditions, whereas  
31 detailed geological conditions and processes for the reduction in natural rocks are  
32 hitherto poorly understood. Here, we report carbonate reduction and genesis of  
33 abiotic methane in dolomitized serpentinites (referred to as ophidolomites) from  
34 a fossil subduction zone (SW Tianshan, China). Detailed petrological, Raman  
35 spectroscopic, strontium and carbon isotopic, and thermodynamic results provide  
36 evidence for dolomite reduction into the phase assemblage of calcite + brucite +  
37 methane, likely associated with retrograde serpentinization starting at 7–9 kbar  
38 and 410–430 °C in the subduction zone. Microthermometric data for dolomite-  
39 hosted fluid inclusions are consistent with petrographic observations, indicative  
40 of fluid entrapment postdating the onset of dolomite reduction during exhumation.  
41 Model calculations suggest that water-rich fluids characterized by relatively high  
42 hydrogen fugacities can create favorable conditions for the reduction process,  
43 which, however, do not exclude the possibility of carbonate methanation by  
44 hydrogen-rich fluids as reported in previous studies. The widespread occurrence

45 of methane in these rocks gives credence to the intricate redox transformations of  
46 subducted carbon, implying that the elevated hydrogen fugacities may facilitate  
47 abiotic synthesis of methane through dolomite reduction at convergent plate  
48 boundaries. Our work shows that alteration of dolomite-bearing lithologies  
49 represents a potential source for abiotic methane in subduction zones, which may  
50 have implications for the transfer of subducted carbon.

51

52 *Keywords:* Abiotic methane; Dolomite reduction; Ophicarbonates; Hydrogen  
53 fugacity; Subduction zone; Chinese southwestern Tianshan

54

## 55 **1. INTRODUCTION**

56 Redox transformations in subduction zones regulate the valence of carbon  
57 (C), and thus control the long-term fate of subducted C (e.g., [Hayes and](#)  
58 [Waldbauer, 2006](#); [Evans, 2012](#); [Galvez and Pubellier, 2019](#); [Tumiati and](#)  
59 [Malaspina, 2019](#); [Sheik et al., 2020](#)). Carbonation of subduction-zone rocks at  
60 forearc to subarc depths by interactions with slab-derived carbon dioxide (CO<sub>2</sub>)-  
61 bearing fluids gives insights into C sequestration under oxidized conditions  
62 ([Tumiati et al., 2013](#); [Piccoli et al., 2016, 2018](#); [Scambelluri et al., 2016](#); [Jaeckel](#)  
63 [et al., 2018](#); [Sieber et al., 2018, 2020](#); [Peng et al., 2020](#); [Hu et al., 2021](#)). On the  
64 other hand, reduction of carbonate minerals at convergent plate boundaries  
65 generates graphite and/or hydrocarbons such as methane (CH<sub>4</sub>), modulating the  
66 distribution of subducted C between solid and fluid inventories ([Malvoisin et al.,](#)

67 2012; Galvez et al., 2013a, b; Vitale Brovarone et al., 2017; Tao et al., 2018a;  
68 Giuntoli et al., 2020). Graphite formation through carbonate reduction during  
69 shallow subduction offers a potential mechanism to retain C in subducted slabs,  
70 which may facilitate C transport into the deep Earth (Malvoisin et al., 2012;  
71 Galvez et al., 2013a, b). In contrast, the release of CH<sub>4</sub> from subducted  
72 ophicalcites (Western Alps, Italy; Vitale Brovarone et al., 2017; Giuntoli et al.,  
73 2020) and carbonated eclogites (SW Tianshan, China; Tao et al., 2018a),  
74 attributed to hydrogen (H<sub>2</sub>)-induced reduction of calcite (referred to as carbonate  
75 methanation; Etiope and Sherwood Lollar, 2013 and references therein) and  
76 aqueous reduction of ferroan dolomite, respectively, provides evidences for  
77 mobile deep C reservoirs. Moreover, olivine-hosted secondary CH<sub>4</sub>-bearing fluid  
78 inclusions were observed in partially serpentized rocks within and above  
79 subducted slabs, interpreted as being due to the reduction of C-bearing species in  
80 metamorphic fluids through subduction-zone serpentization (Sachan et al., 2007;  
81 Vitale Brovarone et al., 2020; Boutier et al., 2021). Therefore, investigating  
82 mechanisms for abiotic CH<sub>4</sub> generation in subduction zones is helpful to our  
83 comprehension of the transfer of slab C.

84 Abiotic CH<sub>4</sub> has been increasingly identified during the past decades,  
85 particularly at shallow geodynamic settings (such as in mid-ocean ridge  
86 hydrothermal systems; e.g., Kelley et al., 2001, 2005), revealing its more  
87 extensive distribution than conventionally assumed (Etiope and Sherwood Lollar,  
88 2013; Etiope and Schoell, 2014). In submarine environments, the hydration of

89 exposed mantle rocks (referred to as serpentinization) commonly accompanies H<sub>2</sub>  
90 discharge, which may favor the synthesis of abiotic CH<sub>4</sub>—with or without other  
91 short-chain hydrocarbons, such as ethane (C<sub>2</sub>H<sub>6</sub>), propane (C<sub>3</sub>H<sub>8</sub>), and butane  
92 (C<sub>4</sub>H<sub>10</sub>)—via Fischer–Tropsch-type reduction of aqueous CO<sub>2</sub> in seawater (e.g.,  
93 [Charlou et al., 2002, 2010](#); [Proskurowski et al., 2008](#)). Conversely, several  
94 metastable intermediate species (e.g., formates), instead of light hydrocarbons,  
95 have been considered to be predominantly generated by abiotic reduction of  
96 dissolved inorganic C during seawater circulation through ultramafic rocks in the  
97 subsurface ([McCollom et al., 2001](#); [McDermott et al., 2015](#)). Geological  
98 production of these organic compounds plays a potential role in the origin of  
99 chemolithoautotrophic life on Earth and other terrestrial planets (e.g., [McCollom  
100 and Seewald, 2013](#); [McDermott et al., 2015](#); [Ménez, 2020](#); [Truche et al., 2020](#)).  
101 Furthermore, H<sub>2</sub>-induced reduction of C-bearing species by serpentinization  
102 within olivine-hosted fluid inclusions in submarine and subaerial vent systems  
103 likely represents a widespread reservoir of abiotic CH<sub>4</sub> over geological timescales  
104 ([Klein et al., 2019](#); [Grozeva et al., 2020](#)). In contrast, abiotic formation of CH<sub>4</sub> in  
105 subduction zones, which is closely related to the mechanisms of deep C mobility,  
106 has received scarce attention. Experiments demonstrated that abiotic CH<sub>4</sub> can be  
107 generated under subduction zone conditions through reduction of subducted C  
108 (e.g., carbonate minerals, organic matter, and dissolved aqueous organic species;  
109 [Sharma et al., 2009](#); [Lazar et al., 2014](#); [Huang et al., 2017](#); [Li, 2017](#); [Mukhina et  
110 al., 2017](#); [Tao et al., 2018a](#)). However, the manifestations of abiotic CH<sub>4</sub> in natural

111 subduction-zone rocks, as well as the geological conditions and reaction pathways  
112 for its production, have been paid insufficient attention, even though CH<sub>4</sub>-bearing  
113 fluid inclusions are not particularly rare in metamorphic lithologies within and  
114 above subducted slabs (Shi et al., 2005; Sachan et al., 2007; Song et al., 2009;  
115 Arai et al., 2012; Vitale Brovarone et al., 2017, 2020; Tao et al., 2018a; Giuntoli  
116 et al., 2020; Boutier et al., 2021; Zhang et al., 2021).

117 In this contribution, we report dolomite reduction and genesis of abiotic CH<sub>4</sub>  
118 in ophidolomites belonging to the ultramafic unit of Changawuzi in the Chinese  
119 southwestern Tianshan high-pressure–ultrahigh-pressure (HP–UHP)  
120 metamorphic belt. We show and discuss petrology, Raman spectroscopy,  
121 microthermometry, strontium (Sr) and C isotope geochemistry, and  
122 thermodynamic modelling to improve understanding of abiotic CH<sub>4</sub> generation in  
123 subduction zones.

124

## 125 **2. GEOLOGICAL BACKGROUND AND SAMPLES**

126 The Chinese southwestern Tianshan HP–UHP metamorphic belt is located  
127 in the northwest of China and formed due to northward subduction of the Tarim  
128 Plate underneath the Yili–Central Tianshan Plate (Fig. 1A; Zhang et al., 2013).  
129 The spatial distribution of HP–UHP rocks in this metamorphic belt allows the  
130 subdivision of a southern HP sub-belt and a northern, coesite-bearing, UHP sub-  
131 belt (Fig. 1B; Lü and Zhang, 2012; Lü et al., 2012a, b; Zhang et al., 2013). The  
132 current work focuses on the Chinese southwestern Tianshan UHP metamorphic

133 belt, which mainly experienced (1) UHP metamorphism (~30 kbar and ~500 °C)  
134 at ca. 320 Ma, (2) peak temperature metamorphism at HP conditions during  
135 exhumation (i.e., thermal relaxation; ~22 kbar and ~600 °C) at ca. 310–315 Ma,  
136 and (3) multistage exhumation to relatively shallow depths (from eclogite facies  
137 to greenschist facies) (Tan et al., 2017; Zhang et al., 2019 and references therein).

138 The main rock types in the Chinese southwestern Tianshan HP–UHP  
139 metamorphic belt are garnet–phengite schists, marbles, blueschists, eclogites, and  
140 serpentinites with associated rodingites (e.g., Shen et al., 2015). Serpentinites are  
141 mostly exposed at Changawuzi in an area of about 6–10 km<sup>2</sup> (Fig. 1C), recording  
142 two stages of serpentinization: (1) a seawater-related hydration process of oceanic  
143 mantle rocks overprinted by the UHP metamorphism ( $37 \pm 7$  kbar and  $520 \pm 10$   
144 °C) during subduction (Shen et al., 2015) and (2) a later rehydration process of  
145 metamorphic and/or primary olivine and pyroxene during exhumation (i.e.,  
146 retrograde serpentinization) starting at 7–9 kbar and 410–430 °C and propagating  
147 to lower *P–T* conditions (Li et al., 2007, 2010). Carbonated serpentinites,  
148 including HP ophidolomites and low-pressure (LP) ophimagnesites and  
149 listvenites, occur in association with the serpentinites and record two carbonation  
150 processes that happened at different stages of exhumation from a depth of ~70 km  
151 to relatively shallow crustal levels (Peng et al., 2020).

152 The herein studied CH<sub>4</sub>-bearing ophidolomites are intimately associated with  
153 (carbonated) serpentinites in the Changawuzi ultramafic blocks (Fig. 1C), which  
154 are surrounded by mica schists (for detailed field occurrence, see Peng et al.,

155 2020). These ophidolomites are characterized by discontinuous and folded  
156 dolomite veins hosted in serpentinites, in which dolomite is encircled by  
157 yellowish calcite and brucite (Fig. 2A and B). Other than the studied samples at  
158 Changawuzi, CH<sub>4</sub>-bearing fluid inclusions were also reported in carbonated  
159 eclogites in adjacent localities of Kebuerte and Habutengsu (Fig. 1B; Tao et al.,  
160 2018a), indicating a relatively widespread distribution of CH<sub>4</sub> in the Chinese  
161 southwestern Tianshan HP–UHP metamorphic belt.

162

### 163 3. METHODS

#### 164 3.1. Scanning electron microscopic analyses

165 Back-scattered electron (BSE) images and compositional X-ray maps were  
166 obtained using an FEI Quanta 650 FEG scanning electron microscope (SEM)  
167 equipped with an Oxford INCA X-MAX50 250+ energy dispersive X-ray  
168 spectrometer at the School of Earth and Space Sciences (SESS), Peking  
169 University. The running conditions were set to an acceleration voltage of 10 kV,  
170 a beam current of 5 nA, and a working distance of ~10 mm. Compositional X-ray  
171 maps were recorded with an integration time of ~360 min.

#### 172 3.2. Electron microprobe analyses

173 Mineral compositions were analyzed using a JEOL 8230 electron  
174 microprobe analyzer at SESS, Peking University. The SPI 53 mineral standards  
175 (U.S.) were adopted for the quantitative analyses (following Li et al., 2018):  
176 jadeite for sodium (Na), aluminium (Al), and silicon (Si); rutile for titanium (Ti);



177 chromium oxide for chromium (Cr); hematite for iron (Fe); rhodonite for  
178 manganese (Mn); diopside for magnesium (Mg) and calcium (Ca); sanidine for  
179 potassium (K); and nickel silicide for nickel (Ni). The acceleration voltage and  
180 beam current were 15 kV and 10 nA, respectively. The beam diameter was 2  $\mu\text{m}$   
181 for all minerals except for calcite (5–10  $\mu\text{m}$ ). The PRZ correction was performed  
182 at the final calibration stage.

### 183 **3.3. Raman spectroscopic and microthermometric analyses**

184 Raman spectra were acquired using a Renishaw InVia Reflex  
185 microspectrometer at SESS, Peking University. Measurements were conducted  
186 on polished thin sections (30  $\mu\text{m}$  thick for mineral analyses and 100  $\mu\text{m}$  thick for  
187 fluid inclusion analyses) without any glue or resin. The laser (532 nm) was  
188 focused on the sample by a DMLM Leica microscope with a 100-fold objective  
189 (numerical aperture (N.A.) = 0.85). Different laser powers were set from an initial  
190 50 mW source for opaque minerals (10%), silicates (50%–100%), carbonates  
191 (50%–100%), and fluid inclusions (100%). The spectrometer was calibrated with  
192 a synthetic Si wafer.

193 Fluid inclusion microthermometric studies were carried out using a Linkam  
194 THMSG 600 heating–freezing stage mounted onto an Olympus microscope at  
195 Key Laboratory of Mineral Resources, Institute of Geology and Geophysics,  
196 Chinese Academy of Sciences (IGGCAS). The two-phase (vapor and liquid) fluid  
197 inclusions with relatively large sizes were selected to determine the final ice  
198 melting temperatures and homogenization temperatures. The heating rates of 0.1–

199 0.2 °C/min were adopted for the determination when phase transitions were  
200 approached. The estimated errors in the measurements are  $\pm 0.1$  °C for the melting  
201 temperatures and  $\pm 2$  °C for the homogenization temperatures. Salinities,  
202 pressures at homogenization, and isochore slopes for the fluid inclusions were  
203 calculated using the procedures described by [Steele-MacInnis et al. \(2012\)](#).

#### 204 **3.4. *In situ* Sr isotopic analyses**

205 *In situ* Sr isotopic measurements of dolomite and calcite were performed by  
206 Nu Plasma II MC-ICP-MS coupled with a 193-nm ArF excimer laser ablation  
207 system (GeoLas HD) at SESS, Peking University (see [Lin et al., 2021](#) for detailed  
208 description of the instrument and laser ablation system). Instrumental operating  
209 conditions and data acquisition protocols are similar to those described in [Ramos](#)  
210 [et al. \(2004\)](#) and [Yang et al. \(2009\)](#). The laser ablation was performed using a spot  
211 size of  $\sim 90$   $\mu\text{m}$ , a repetition rate of  $\sim 5$  Hz, and an energy density of  $\sim 10$  J/cm<sup>2</sup>.  
212 The helium (He) gas (with a flow rate of  $\sim 0.5$  L/min), carrying ablated sample  
213 aerosols and passing through the “wire” signal smoothing device ([Hu et al., 2012](#)),  
214 was merged with argon (Ar) gas before entering the plasma. Prior to each ablation,  
215 a 30-s measurement of gas blank was employed to correct for the isobaric  
216 interference of krypton (Kr). Correction of rubidium (Rb) was conducted using  
217 the natural ratio of  $^{85}\text{Rb}/^{87}\text{Rb} = 2.5926$  with an exponential law, assuming that the  
218 mass bias of Rb is identical to that of Sr (e.g., [Woodhead et al., 2005](#)). Actually,  
219 the studied samples have extremely low  $^{87}\text{Rb}/^{86}\text{Sr}$  values, indicative of the  
220 negligible interference of Rb. Previous studies have demonstrated that the

221 interference of Ca argides and dimers in carbonate minerals is minor and thus has  
222 insignificant influence on the accuracy of  $^{87}\text{Sr}/^{86}\text{Sr}$  ratios (e.g., [Ramos et al., 2004](#);  
223 [Vroon et al., 2008](#); [Yang et al., 2009](#)). Double-charged ions in the samples have  
224 extremely low ion signals, suggesting that they play a very limited role in  
225 interfering  $^{87}\text{Sr}/^{86}\text{Sr}$  ratios. The instrumental mass bias was corrected using the  
226  $^{86}\text{Sr}/^{88}\text{Sr}$  ratio of 0.1194 with an exponential law. A modern Porites coral (Hainan  
227 Island, China) was used as the internal standard to evaluate the accuracy of the  
228 analyses, which yielded  $^{87}\text{Sr}/^{86}\text{Sr}$  ratios of  $0.709170 \pm 0.000016$  ( $2\sigma$ ,  $n = 33$ ), in  
229 agreement with those obtained by solution-based MC-ICP-MS analyses ( $^{87}\text{Sr}/^{86}\text{Sr}$   
230 =  $0.709176 \pm 0.000016$ ; [Yang et al., 2009](#)). In this study, Sr isotope data with  
231 generally comparable  $^{88}\text{Sr}$  ion signals higher than  $\sim 1$  V were selected for dolomite  
232 and calcite to minimize the potential influence of composition-induced matrix  
233 effects and brucite interference on calcite due to their intergrown textures ([Section](#)  
234 [4.1](#)). In general, the analyzed  $^{87}\text{Sr}/^{86}\text{Sr}$  ratios of dolomite are close to those  
235 obtained by solution-based TIMS analyses for dolomite in surrounding HP  
236 ophidolomites ([Section 4.3](#); [Peng et al., 2020](#)).

### 237 **3.5. C and O isotopic analyses**

238 Microdrilling was conducted on dolomite and calcite using a standard dentist  
239 drill (0.2 mm, 0.5 mm, and 1.0 mm) under the stereomicroscope (SMZ 1500) at  
240 State Key Laboratory of Lithospheric Evolution (SKLLE), IGGCAS. Vertical  
241 holes were drilled down to thick sections (ca. 0.3–0.5 mm) by increments and at  
242 least 2 mg of powder of each selected grain was collected. C and O isotope

243 compositions of dolomite, calcite, and bulk carbonate were determined using a  
244 Thermo Fisher MAT 253 isotope ratio mass spectrometer coupled with a  
245 GasBench II peripheral device at SKLLE, IGGCAS, through production of CO<sub>2</sub>  
246 after reaction with phosphoric acid. The reaction vial was automatically flushed  
247 with high-purity (99.999%) He gas for 10 min at a flow rate of ~0.1 L/min to  
248 remove atmospheric contaminants including traces of CO<sub>2</sub> and water (H<sub>2</sub>O) vapor.  
249 The acid digestion was performed in the GasBench II using continuous flow mode  
250 at a temperature of 70 °C, through which the generated CO<sub>2</sub> was transferred by  
251 the He carrier gas into the mass spectrometer. In the analyses, δ<sup>18</sup>O values of bulk  
252 carbonate were not reported because the mixture of dolomite and calcite prevents  
253 the accurate back-calculation by using O isotope fractionation factors between the  
254 carbonate and phosphoric acid. Standard deviations of δ<sup>13</sup>C and δ<sup>18</sup>O values were  
255 calculated from replicate analyses of an internal laboratory calcite standard, which  
256 are better than 0.15‰ and 0.20‰, respectively. The measured δ<sup>13</sup>C and δ<sup>18</sup>O  
257 values are reported relative to the Vienna Pee Dee Belemnite (V-PDB) and  
258 Vienna Standard Mean Ocean Water (V-SMOW), respectively.

### 259 **3.6. Thermodynamic modelling**

260 To evaluate the role of oxygen fugacity ( $fO_2$ ; log bar unit) and hydrogen  
261 fugacity ( $fH_2$ ; log bar unit) in the reduction process of dolomite (nearly pure;  
262 [Section 4.1](#)), we calculated the  $fO_2$ - $fH_2$  equilibrium diagram in the Ca-Mg-C-O-  
263 H system (with fixed Ca:Mg:C of 1:1:2 in molar ratio) at 8 kbar and 420 °C using  
264 Perple\_X software (version 6.7.4; [Connolly, 2005](#)) and the internally consistent

265 thermodynamic database of [Holland and Powell \(1998\)](#) revised in 2004  
266 (hp04ver.dat). The  $P$ – $T$  conditions were chosen based on the onset of retrograde  
267 serpentinization in the Tianshan ([Li et al., 2007, 2010](#)). Thermodynamic  
268 parameters of phases belonging to the system are provided in [Supplementary](#)  
269 [Table S1](#), most of which are available from literatures ([Robie and Hemingway,](#)  
270 [1995; Holland and Powell, 1998; Fukui et al., 2003](#)) while the thermal expansion  
271 coefficient of portlandite was calculated based on the cell volume changes during  
272 heating from [Xu et al. \(2007\)](#). Redox buffers of magnetite–hematite (MH),  
273 fayalite–magnetite–quartz (FMQ), and iron–magnetite (IM) were calculated for  
274 reference at 8 kbar and 420 °C. The thermodynamic model of H<sub>2</sub>O was performed  
275 using the Fluids routine (H–O MRK hybrid–EoS) of the Perple\_X software,  
276 which will be discussed in [Section 4.4](#).

277 To investigate the equilibrated phase assemblages of reduced ophidolomites  
278 during the retrograde serpentinization, we computed  $P$ – $T$  pseudosections for a  
279 representative sample C1534 in the Ca–Fe–Mg–Si–C–O–H system. The applied  
280 solid solution models and their sources are provided in [Supplementary Table S2](#).  
281 The bulk-rock composition used for the pseudosections was measured by X-ray  
282 fluorescence (XRF) spectrometry at the National Research Center for Geoanalysis,  
283 Chinese Academy of Geological Science. The contents of major oxides and loss  
284 on ignition (LOI) are listed in [Table 1](#), with the analytical uncertainties better than  
285 5%. To specify C as the thermodynamic components, we further derived the  
286 effective bulk-rock composition ([Table 1](#)) by integrating mineral compositions

287 and modes, in which the H<sub>2</sub>O and CO<sub>2</sub> contents were calculated based on the  
288 abundances of hydrous minerals and carbonates in the sample (see [Li et al., 2012](#)  
289 and [Peng et al., 2020](#) for similar approaches).

290

## 291 **4. RESULTS**

### 292 **4.1. Petrography and mineral chemistry of ophidolomites**

293 The studied ophidolomites consist primarily of antigorite and dolomite,  
294 while calcite, brucite, magnetite, and olivine are present as minor or accessory  
295 phases. Microstructures show a replacement texture in which dolomite grows at  
296 the expense of antigorite ([Fig. 2C and D](#)). In most cases, dolomite grains have  
297 experienced various degrees of decomposition, resulting in the formation of  
298 acicular calcite–brucite intergrowths ([Fig. 2E–G](#)). This transformation propagates  
299 inside dolomite along microcracks ([Fig. 2G](#)), which, together with patches of  
300 relict dolomite in calcite products ([Fig. 2H](#)), suggests the retrograde  
301 decomposition postdating dolomite formation. Olivine occurs as relicts in the  
302 antigorite matrix ([Fig. 3A](#)) and inclusions (in association with antigorite and  
303 brucite) within magnetite ([Fig. 3B and C](#)). Magnetite grains, ranging in size from  
304 one to several millimeters, commonly enclose a variety of minerals that are  
305 dominated by antigorite and dolomite ([Fig. 3B](#)). In some of the magnetite-hosted  
306 mineral inclusions, the replacement of dolomite by calcite and brucite are  
307 observed ([Fig. 3D](#)).

308 Representative mineral compositions of the studied ophidolomites are  
309 presented in [Table 2](#). Antigorite and dolomite show nearly identical  $X_{\text{Mg}}$  (=  $\text{Mg}/(\text{Mg} + \text{Fe})_{\text{molar}}$ ) values of 0.958–0.985 and 0.955–0.991 ([Supplementary Fig. S1](#)), respectively, in agreement with the petrographically recognized dolomite  
311 growth at the expense of antigorite ([Fig. 2C and D](#)). Also, the acicular brucite  
312 intergrown with calcite exhibits similar  $X_{\text{Mg}}$  values of 0.963–0.992  
313 ([Supplementary Fig. S1](#)), in accord with the petrographic identification of  
314 dolomite transformation into calcite and brucite ([Fig. 2E–H](#)). By contrast, olivine  
315 displays relatively lower  $X_{\text{Mg}}$  values of 0.932–0.933, comparable to those of  
316 metamorphic olivine ( $X_{\text{Mg}} = 0.91\text{--}0.93$ ) in associated UHP serpentinites  
317 ([Supplementary Fig. S1](#); [Shen et al., 2015](#)).

#### 319 **4.2. Petrography, Raman spectroscopy, and microthermometry of fluid** 320 **inclusions**

321 Abundant fluid inclusions, variable in both shapes (spherical, sub-spherical,  
322 and tubular) and sizes (from submicron to  $\sim 8\ \mu\text{m}$ ), are observed in dolomite in the  
323 studied ophidolomites. These fluid inclusions are grouped into fluid inclusion  
324 assemblages (FIAs) based on petrographic criteria ([Goldstein and Reynolds, 1994](#);  
325 [Bodnar, 2003](#)), and two main types of FIAs are further distinguished at room  
326 temperatures. Fluid inclusions in the pervasive Type-I FIAs contain vapor and  
327 liquid phases and show weak optical contrast to dolomite ([Fig. 4A and B](#)).  
328 Typically, these two-phase fluid inclusions are liquid-rich and have less variable  
329 vapor to liquid ratios of about 5–15 vol% ([Fig. 4A and B](#)). Conversely, fluid

330 inclusions in Type-II FIAs commonly contain a single phase and show strong  
331 optical contrast to dolomite (Fig. 4C and D). In most cases, both types of FIAs  
332 form trails crosscutting grain boundaries (Fig. 4A–D), indicating their entrapment  
333 later than the host dolomite. However, the cloudy appearance and fine grain sizes  
334 of calcite–brucite intergrowths (Fig. 2E–H) have significantly hindered the  
335 recognition of calcite-hosted fluid inclusions. Despite this, two-phase fluid  
336 inclusions are observed in calcite owing to the movement of vapor bubbles inside,  
337 which are mostly isolated and randomly distributed, probably reflecting fluid  
338 entrapment during the growth of calcite (Fig. 4E–G and Supplementary Fig. S2A  
339 and B).

340 Raman spectroscopic and microthermometric studies were conducted on the  
341 fluid inclusions. In Type-I fluid inclusions, the gaseous and liquid species are rich  
342 in CH<sub>4</sub> and H<sub>2</sub>O, respectively, whereas the strong fluorescence interference of the  
343 host carbonates sometimes impedes direct observation of the H<sub>2</sub>O peaks (Fig. 5A  
344 and B; see also Yang et al., 2018). In contrast, dolomite-hosted Type-II fluid  
345 inclusions certainly contain CH<sub>4</sub>, while H<sub>2</sub> was occasionally detected (Fig. 5C).  
346 In rare cases, calcite and brucite were detected in only a few of dolomite-hosted  
347 Type-II fluid inclusions, which, however, cannot be unequivocally considered as  
348 daughter minerals (Supplementary Fig. S2C). Overall, Type-I vapor- and liquid-  
349 bearing fluid inclusions show relatively consistent final ice melting temperatures  
350 ( $T_m$ ) of –3.6 to –1.3 °C, corresponding to salinities of 2.2–5.9 wt% NaCl (Table  
351 3). Moreover, these two-phase fluid inclusions have generally comparable



352 homogenization temperatures ( $T_h$ ) of 180–230 °C, pressures at homogenization  
353 ( $P_h$ ) of 9–27 bar, and isochore slopes ( $dP/dT$ ) of 14.2–17.0 (Table 3).

### 354 4.3. Isotope geochemistry

355 Representative Sr isotope compositions of dolomite and calcite in the studied  
356 ophidolomites are listed in Table 4. Dolomite has  $^{87}\text{Sr}/^{86}\text{Sr}$  ratios of 0.70476–  
357 0.70757 (average = 0.70566,  $n = 50$ ), lower than those of Ordovician–  
358 Carboniferous (lifetime of the south Tianshan paleo-ocean; Xia et al., 2014)  
359 seawater ( $^{87}\text{Sr}/^{86}\text{Sr} = \text{ca. } 0.7076\text{--}0.7092$ ; Veizer et al., 1999) but similar to those  
360 of associated HP ophidolomites and their dolomite separates ( $^{87}\text{Sr}/^{86}\text{Sr} = \text{ca.}$   
361 0.7064–0.7075; Peng et al., 2020) (Fig. 6A). In contrast, calcite shows relatively  
362 higher  $^{87}\text{Sr}/^{86}\text{Sr}$  ratios of 0.70867–0.70986 (average = 0.70938,  $n = 46$ ), which are  
363 comparable to those of the seawater as well as serpentinites in the Tianshan (Peng  
364 et al., 2020) (Fig. 6A).

365 Detailed C and O isotope values of dolomite, calcite, and bulk carbonate in  
366 the studied ophidolomites are shown in Table 5. Dolomite and calcite have  $\delta^{13}\text{C}$   
367 values of +9.2‰ ~ +11.7‰ and +7.0‰ ~ +9.0‰, respectively, similar to those of  
368 bulk carbonate ( $\delta^{13}\text{C} = +8.6\text{‰} \sim +10.3\text{‰}$ ) (Fig. 6B). These C isotope values are  
369 significantly higher than  $\delta^{13}\text{C}$  of marine carbonates (–3‰ ~ +3‰; Hoefs, 2009)  
370 and carbonate-bearing but CH<sub>4</sub>-absent lithologies from the Tianshan (mostly ≤  
371 0‰; van der Straaten et al., 2012; Collins et al., 2015; Peng et al., 2018, 2020;  
372 Zhu et al., 2018) (Fig. 6B). Moreover, dolomite and calcite display  $\delta^{18}\text{O}$  values of  
373 +8.1‰ ~ +9.6‰ and +8.4‰ ~ +12.6‰, respectively (Fig. 6B).

#### 374 4.4. Thermodynamic results

375 In the  $f\text{O}_2$ - $f\text{H}_2$  equilibrium diagram of Fig. 7A, the stability field of dolomite,  
376 shrinking with the elevated  $\log f\text{H}_2$  values, extends down to  $\log f\text{O}_2 = -29.1$   
377 ( $\Delta\text{FMQ} -2.5$ , where  $\Delta\text{FMQ}$  refers to the deviation of  $\log f\text{O}_2$  from the FMQ buffer)  
378 at  $\log f\text{H}_2 < 1.4$ . The boundary between dolomite and the phase assemblage of  
379 calcite + brucite +  $\text{CH}_4$  is constrained at  $\log f\text{O}_2 = -27.3 \sim -20.6$  ( $\Delta\text{FMQ} -0.7 \sim$   
380  $+6.0$ ) and  $\log f\text{H}_2 = 0.3 \sim 1.4$ . In the H-O system, pure  $\text{H}_2\text{O}$  ( $y_{\text{H}_2\text{O}} = 1$ , where  $y_{\text{H}_2\text{O}}$   
381 is the molar fraction of  $\text{H}_2\text{O}$  in fluids) is characterized by an ideal  $X_{\text{O}}$  ( $= \text{O}/(\text{O} +$   
382  $\text{H})_{\text{molar}}$ ) of  $1/3$ . In the vicinity of this value, only negligible amounts of  $\text{O}_2$  or  $\text{H}_2$  is  
383 encompassed due to the  $f\text{O}_2$ - and  $f\text{H}_2$ -dependent  $\text{H}_2\text{O}$  dissociation, representing  
384 slightly oxidized or reduced conditions, respectively (e.g., Connolly, 1995). In  
385 this study, we superposed the thermodynamically calculated model of slightly  
386 reduced  $\text{H}_2\text{O}$  at  $X_{\text{O}} = 0.33 \sim 1/3$  on the  $f\text{O}_2$ - $f\text{H}_2$  diagram (Fig. 7A), based on the  
387 inferred serpentinization-derived fluids responsible for dolomite reduction  
388 (Section 5.2) and the widely distributed aqueous fluid inclusions but the  
389 sporadically detected  $\text{H}_2$  in the studied rocks (Figs. 4 and 5; Section 4.2). Although  
390 the reactive reduced fluids may potentially contain small amounts of other  
391 components (see below), they do not significantly affect our model calculations  
392 performed in the H-O system. Firstly, the fluids are likely  $\text{CO}_2$ -poor, because  
393 fluid inclusions do not contain detectable  $\text{CO}_2$  in the studied ophidolomites and  
394 carbonate minerals are not widely distributed in surrounding rodingites formed by  
395 interactions with fluids related to the retrograde serpentinization (Li et al., 2007,

396 [2010; Shen et al., 2012, 2016](#)). Alternatively, preexisting C-bearing species (e.g.,  
397 CO<sub>2</sub>) in the fluids may have been reduced into CH<sub>4</sub> during the serpentinization,  
398 as recorded in partially serpentinized rocks in comparable metamorphic settings  
399 ([Sachan et al. 2007; Vitale Brovarone et al., 2020; Boutier et al., 2021](#)). In this  
400 scenario, we set C concentrations of 0.001–0.05 molal in the fluids equilibrated  
401 with carbonate-undersaturated to carbonate-saturated serpentinites at the studied  
402 *P–T* conditions ([Vitale Brovarone et al., 2020](#)), and the calculated mole fractions  
403 of H<sub>2</sub>O are significantly higher than those of other molecular species (e.g., CH<sub>4</sub>,  
404 CO<sub>2</sub>, and H<sub>2</sub>) at *X*<sub>O</sub> close to 1/3 ([Supplementary Fig. S3](#)). Secondly, even though  
405 halogens (e.g., chlorine, Cl) commonly occur in serpentinizing fluids that may  
406 decrease the activity of H<sub>2</sub>O (e.g., [Lamadrid et al., 2017, 2021](#)), CH<sub>4</sub>-bearing  
407 aqueous fluid inclusions in the studied rocks contain relatively low salinities of  
408 2.2–5.9 wt% NaCl ([Table 3](#)). These salinities correspond to H<sub>2</sub>O mole fractions  
409 of ca. 0.981–0.993 in the fluids, and thus have a negligible effect on the activity  
410 of H<sub>2</sub>O (e.g., [Aranovich and Newton, 1996](#)). Thirdly, thermodynamic calculations  
411 predicted very low electrolyte concentrations of ca. 0.004–0.03 molal (mainly Si,  
412 Mg, and Ca) in the fluids equilibrated with the Tianshan serpentinites during  
413 retrogression ([Supplementary Fig. S4](#)), indicating that these electrolytic solutes  
414 cannot profoundly affect the homogeneous equilibria among the dominant  
415 molecular species and thus the application of molecular fluid models ([Connolly  
416 and Galvez, 2018](#)). It is therefore likely that the possible existence of dissolved  
417 species (e.g., CO<sub>2</sub>, Cl, and other electrolytes) in the reactive reduced fluids have

418 only minor effects on the calculations in our model. The  $f\text{O}_2$ - $f\text{H}_2$  equilibrium  
419 diagram illustrates that an infiltration of  $\text{H}_2\text{O}$ -rich fluids characterized by  
420 relatively high  $f\text{H}_2$  values can contribute to abiotic  $\text{CH}_4$  formation through  
421 dolomite reduction at the studied  $P$ - $T$  conditions (Fig. 7A). For instance, at  $X_{\text{O}} =$   
422 0.3333323 (corresponding to  $y_{\text{H}_2\text{O}} = 0.999995$  and  $y_{\text{H}_2} = 0.000005$ ; star in Fig. 7A),  
423 the  $\text{H}_2\text{O}$ -rich fluids buffered at  $\log f\text{O}_2 = -26.0$  ( $\Delta\text{FMQ} + 0.6$ ) show a  $\log f\text{H}_2$  value  
424 of 0.8 and equilibrate with the phase assemblage of calcite + brucite +  $\text{CH}_4$ .

425 The calculated  $P$ - $T$  pseudosection for the reduced ophidolomite (Sample  
426 C1534) at  $\log f\text{O}_2 = -26.0$  and  $\log f\text{H}_2 = 0.8$  (star in Fig. 7A) suggests that the  
427 observed phase assemblage of antigorite + brucite + calcite + magnetite +  $\text{CH}_4$   
428 can be predicted at 7–9 kbar and 410–430 °C (Fig. 7B). Similar results computed  
429 at  $\log f\text{O}_2 = -25.8$  and  $\log f\text{H}_2 = 0.7$  (Supplementary Fig. S5A) indicate that  
430 variable  $f\text{O}_2$  and  $f\text{H}_2$  of the fluids in equilibrium with calcite + brucite +  $\text{CH}_4$  have  
431 no significant effects on the  $P$ - $T$  pseudosection. However, since the constrained  
432  $\log f\text{O}_2$  and  $\log f\text{H}_2$  values for these calculations depend on and vary with  $P$ - $T$   
433 conditions, uncertainties may occur in the phase stabilities predicted at  $P$ - $T$   
434 conditions considerably higher or lower than 7–9 kbar and 410–430 °C in Fig. 7B  
435 and Supplementary Fig. S5A. Further, the  $P$ - $T$  pseudosection was calculated for  
436 the sample without  $f\text{O}_2$  and  $f\text{H}_2$  constraints, demonstrating that the unreduced  
437 mineral assemblage of antigorite + brucite + dolomite + calcite + magnetite can  
438 remain stable at the studied  $P$ - $T$  conditions (Supplementary Fig. S5B).

439

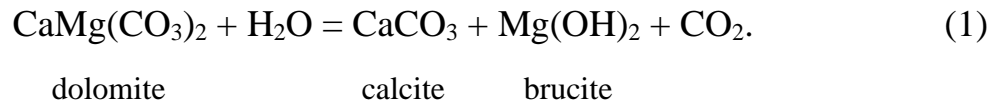
## 440 5. DISCUSSION

441 Ophicarbonates play a potential role in contributing to the subduction influx  
442 of C (Dasgupta and Hirschmann, 2010; Alt et al., 2012, 2013) and recording the  
443 mechanisms of C mobility and percolation at convergent plate boundaries  
444 (Scambelluri et al., 2016; Vitale Brovarone et al., 2017; Piccoli et al., 2018;  
445 Cannà et al., 2020; Peng et al., 2020). Marine-originated ophicarbonates (mainly  
446 ophicalcites) are typically characterized by Ca-carbonate matrix cementing  
447 serpentinite clasts or Ca-carbonate veins filling fractured serpentinites (Bonatti et  
448 al., 1974; Früh-Green et al., 2003; Schwarzenbach et al., 2013; Clerc et al., 2014;  
449 Lafay et al., 2017). Subseafloor mixing zones between these pristine ophicalcites  
450 and serpentinites may have served as incubators for biological communities in the  
451 hydrated oceanic mantle, offering insights into deep chemolithoautotrophic life  
452 (Klein et al., 2015). Moreover, *HP* carbonation of subduction-zone serpentinites  
453 through interactions with slab-released CO<sub>2</sub>-bearing fluids has been increasingly  
454 recognized, providing implications for the distribution of subducted C  
455 (Scambelluri et al., 2016; Piccoli et al., 2018; Peng et al., 2020). The Changawuzi  
456 *HP* ophidolomites (15–25 kbar and 550–600 °C) have been studied in detail by  
457 Peng et al. (2020), which are characterized by carbonate growth at the expense of  
458 silicates in the host serpentinites and record interactions with CO<sub>2</sub>-bearing fluids  
459 emanating from metamafic and/or metasedimentary rocks in the subduction zone.  
460 Similarly, the replacement of metamorphic antigorite by dolomite (Fig. 2C and D)  
461 and their compositional inheritance (e.g.,  $X_{Mg}$  values; Supplementary Fig. S1) in

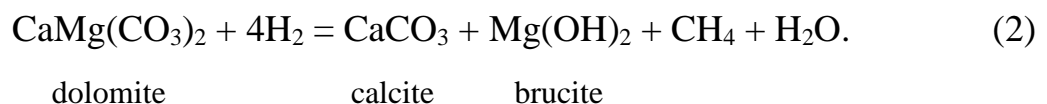
462 the studied CH<sub>4</sub>-bearing ophidolomites point to dolomite formation through  
463 interactions between CO<sub>2</sub>-bearing fluids and serpentinites during metamorphism.  
464 This is reflected by Sr isotope compositions of dolomite in these rocks  
465 considerably distinct from those of seawater in the south Tianshan paleo-ocean  
466 but generally similar to those of associated HP ophidolomites and their dolomite  
467 separates (Fig. 6A), likely inheriting the low <sup>87</sup>Sr/<sup>86</sup>Sr values of subducted  
468 carbonate-bearing lithologies in the Tianshan (Peng et al., 2020). Microstructures,  
469 mineral compositions, and Sr isotopic signatures of the studied CH<sub>4</sub>-bearing  
470 ophidolomites are comparable to those of HP ophidolomites in the same study  
471 area (Peng et al., 2020), indicating that they likely record the consistent HP  
472 carbonation of serpentinites in the subduction zone. Even though obtaining  
473 precise *P–T* constraints for dolomite formation in the studied rocks is relatively  
474 difficult, it may not considerably affect the following discussion with respect to  
475 dolomite reduction and abiotic CH<sub>4</sub> generation in the subduction zone.

### 476 **5.1. Abiotic CH<sub>4</sub> generation through dolomite reduction**

477 Intergrowths of calcite and brucite in natural rocks (Fig. 2E–H) are relatively  
478 hard to be preserved because these fine and soluble minerals are easily removed  
479 by an abundance of circulating fluids (Berg, 1986). The retrograde decomposition  
480 of dolomite into calcite–brucite intergrowths was observed in mantle wedge  
481 ultramafic rocks and interpreted as Reaction (1), which occurred by infiltration of  
482 H<sub>2</sub>O at oxidized conditions (Förster et al., 2017; Consuma et al., 2020):



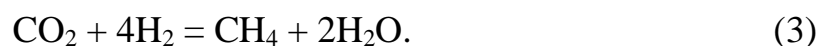
483 In this study, by contrast, the pervasive occurrence of  $\text{CH}_4 \pm \text{H}_2\text{O} \pm \text{H}_2$  in  
 484 dolomite- and calcite-hosted fluid inclusions (Figs. 4 and 5) likely suggests  
 485 reduced aqueous fluids responsible for the decomposition of dolomite.  
 486 Nevertheless, the limited distribution of  $\text{H}_2$  in the fluid inclusions (Section 4.2) is  
 487 probably indicative of its minor proportion in the reactive aqueous fluids, or,  
 488 alternatively, ascribed to several other potential processes (see below).  
 489 Thermodynamic calculations further demonstrate that an infiltration of  $\text{H}_2\text{O}$ -rich  
 490 fluids, characterized by a relatively high  $\log f\text{H}_2$  value of 0.8 but containing a low  
 491  $\text{H}_2$  molar fraction of 0.000005 (star in Fig. 7A), can result in the transformation  
 492 of dolomite into the phase assemblage of calcite + brucite +  $\text{CH}_4$ , which is  
 493 expressed by the  $f\text{H}_2$ -dependent Reaction (2):



494 This  $\text{CH}_4$ -generating reaction is endorsed by the notably high  $\delta^{13}\text{C}$  values of  
 495 carbonates in the studied rocks (Fig. 6B). The positive shift in  $\delta^{13}\text{C}$  is exactly  
 496 opposite to the typical C isotopic trend related to decarbonation reactions and/or  
 497 carbonate–organic matter re-equilibrations as also recorded in the Tianshan (Fig.  
 498 6B; Collins et al., 2015; Zhu et al., 2018). Similar high  $\delta^{13}\text{C}$  values were  
 499 interpreted as evidence for carbonate reduction forming graphite (Galvez et al.,  
 500 2013b) or abiotic  $\text{CH}_4$  (Vitale Brovarone et al., 2017) in comparable metamorphic  
 501 settings. Based on  $\delta^{13}\text{C}$  of calcite (Table 5) and the equilibrium fractionation

502 factor between calcite and CH<sub>4</sub> ( $\ln\alpha(\text{CaCO}_3\text{--CH}_4) = +15.0\text{‰} \sim +16.0\text{‰}$  at 410–  
503 430 °C; [Bottinga, 1969](#)), we calculated C isotope compositions of CH<sub>4</sub> ranging  
504 from –9.0‰ to –6.0‰. These values fit the range of C isotope compositions of  
505 abiotic CH<sub>4</sub> from worldwide occurrences, which display  $\delta^{13}\text{C}$  values typically  
506 higher than ca. –25‰ (e.g., [Ueno et al., 2006](#); [Etiope et al., 2011](#)). Considering  
507 that dolomite in the studied ophidolomites is likely related to the HP carbonation  
508 of serpentinites (see above), its heavy  $\delta^{13}\text{C}$  values relative to those in associated  
509 HP ophidolomites ([Fig. 6B](#)) are probably attributed to an additional reduction  
510 process of dolomite other than Reaction (2). In this process, dolomite may have  
511 been decomposed into CH<sub>4</sub> together with aqueous species such as Ca<sup>2+</sup> and Mg<sup>2+</sup>,  
512 which represents the reduction of dissolved C-bearing species (e.g., CO<sub>3</sub><sup>2-</sup>, HCO<sub>3</sub><sup>-</sup>,  
513 and/or CO<sub>2,aq</sub>) of dolomite (see [Frezzotti et al., 2011](#); [Ague and Nicolescu, 2014](#);  
514 [and Facq et al., 2014](#) for carbonate dissolution in subduction zones). In addition  
515 to the potential dissolution-induced dolomite reduction, other processes resulting  
516 in C isotopic enrichment of the residual dolomite may also be possible.

517 It is apparent that Reaction (2) essentially reflects a H<sub>2</sub>O-triggered  
518 decarbonation process of dolomite (Reaction (1)) coupled with a coinstantaneous  
519  $f\text{H}_2$ -dependent reduction process of CO<sub>2</sub> (Reaction (3)):



520 In this study, however, the decarbonation of dolomite is not spontaneous in  
521 reduced environments and thus seems unlikely to proceed independently prior to  
522 the reduction of CO<sub>2</sub> (see below). Firstly, the fluid inclusions do not contain



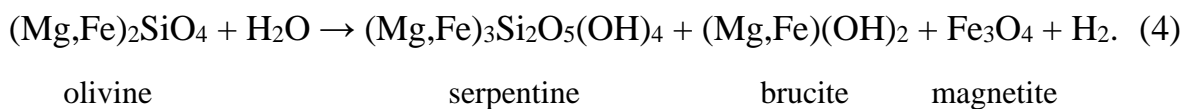
523 detectable CO<sub>2</sub> as the intermediate product, in which CH<sub>4</sub> occurs as the dominant  
524 C-bearing species instead. The isolated and randomly distributed CH<sub>4</sub>-bearing  
525 fluid inclusions in calcite may provide further evidence for the simultaneous  
526 production of CH<sub>4</sub> and calcite through dolomite decomposition (Fig. 4E–G and  
527 [Supplementary Fig. S2A](#) and B). Secondly, the retrograde serpentinization  
528 responsible for abiogenic CH<sub>4</sub> formation ([Section 5.2](#)) started at 7–9 kbar and 410–  
529 430 °C and propagated to lower *P–T* conditions (e.g., 2–10 kbar and 250–350 °C;  
530 [Li et al., 2007, 2010](#)), indicating that dolomite decarbonation, if it exists, should  
531 take place at oxidized conditions prior to the retrograde serpentinization. In this  
532 scenario (i.e., *P* > 7–9 kbar and *T* > 410–430 °C), aragonite is likely to replace  
533 calcite as the dominant Ca-carbonate products (cf. the calcite–aragonite transition  
534 in [Fig. 8](#); [Johannes and Puhan, 1971](#)), inconsistent with the observed calcite–  
535 brucite intergrowths in the studied ophidolomites ([Fig. 2E–H](#)). Thirdly, the  
536 elevated C isotope values of calcite, contrary to the negative shift of δ<sup>13</sup>C derived  
537 from carbonate decarbonation ([Fig. 6B](#)), provide geochemical constraints on the  
538 equilibrium between calcite and CH<sub>4</sub> in the studied ophidolomites (see above).  
539 An alternative explanation may exist for these results that dolomite has recorded  
540 <sup>13</sup>C enrichment (e.g., through dissolution-induced reduction; see above) prior to  
541 the decoupled dolomite decarbonation and CO<sub>2</sub> reduction processes, but such  
542 cyclic redox transformations (i.e., reduction–oxidation–reduction) are not  
543 reported in the study area ([Li et al., 2007, 2010](#)).

544 Although our model calculations demonstrate that H<sub>2</sub>O-rich fluids at  
545 relatively high  $fH_2$  (e.g.,  $y_{H_2O} = 0.999995$  at  $\log fH_2 = 0.8$ ; star in Fig. 7A) can  
546 create favorable conditions for dolomite reduction and abiotic CH<sub>4</sub> generation, the  
547 possibility of carbonate methanation by H<sub>2</sub>-rich fluids cannot be excluded. The  
548 latter case has been reported in subducted ophicalcites in the Western Alps,  
549 recording a H<sub>2</sub>-induced calcite methanation process in which the equilibrated  
550 fluids are characterized by dominant CH<sub>4</sub> while  $y_{H_2O} = y_{H_2}$  at  $X_O < 0.03$  at 7 kbar  
551 and 350 °C (Vitale Brovarone et al., 2017). In this scenario, H<sub>2</sub> is not pervasively  
552 detected by Raman spectroscopy in fluid inclusions in the studied rocks (Figs. 4  
553 and 5; Section 4.2) probably because it has been largely consumed by carbonate  
554 reduction to CH<sub>4</sub> (e.g., Grozeva et al., 2020). Alternatively, H<sub>2</sub> could potentially  
555 occur in the fluid inclusions but the Raman peaks have been severely obscured by  
556 the strong fluorescence of the host carbonates (Fig. 5). Overall, there is no  
557 petrographic evidence for post-entrapment re-equilibrations of the fluid inclusions  
558 (e.g., stretching, leakage, and decrepitation), as supported by their relatively  
559 consistent vapor to liquid ratios (Fig. 4A and B; Section 4.2), homogenization  
560 temperatures (Table 3), and Raman peak positions of gaseous CH<sub>4</sub>  
561 (Supplementary Table S3) within an individual FIA (e.g., Bodnar, 2003; Lin et  
562 al., 2007). Concentrations of molecular species as a function of  $X_O$  in the graphite-  
563 buffered COH system calculated at 7 kbar and 350 °C (Vitale Brovarone et al.,  
564 2017; see Supplementary Fig. S6 for similar calculations at the studied  $P$ - $T$   
565 conditions) illustrate that mole fractions of H<sub>2</sub>O in the fluids, relative to CH<sub>4</sub> and

566 H<sub>2</sub>, progressively increase with X<sub>O</sub> (until at X<sub>O</sub> = 1/3). Such calculations suggest  
567 that determination of proportions of these species in the equilibrated fluids may  
568 provide important insights into the reduced nature of the reactive fluids (i.e., H<sub>2</sub>O-  
569 rich fluids at relatively high *f*H<sub>2</sub> vs. H<sub>2</sub>-rich fluids).

## 570 **5.2. Reduced fluid source(s) and fluid inclusion entrapment**

571 The reactive reduced fluids are likely associated with retrograde  
572 serpentinization in the Tianshan, during which the observed phase assemblage in  
573 the studied rocks can remain stable (Fig. 7B and Supplementary Fig. S5). Even  
574 though fluid source(s) responsible for the retrograde serpentinization is(are)  
575 largely unresolved (Li et al., 2007, 2010), the preservation of Sr and O isotopic  
576 signatures of seawater in the Tianshan serpentinites (Scicchitano et al., 2018; Peng  
577 et al., 2020) suggests that these rocks may record interactions with fluids  
578 migrating upward from serpentinite dehydration at greater depths (see also  
579 Angiboust et al., 2014 and Piccoli et al., 2018). Serpentinization of olivine  
580 provides a potential source for H<sub>2</sub>, together with the concomitant formation of  
581 magnetite (Reaction (4); e.g., McCollom and Bach, 2009; Klein et al., 2013, 2020).



582 Although the possibility for serpentinization of olivine to produce H<sub>2</sub> at high  
583 temperatures (400–600 °C) has been questioned (Evans, 2010), recent studies  
584 show that magnetite formation and H<sub>2</sub> generation through HP serpentinization  
585 may be common under several subduction zone conditions (Vitale Brovarone et

586 al., 2020; Boutier et al., 2021). Thus, olivine relicts in the antigorite matrix (Fig.  
587 3A), as well as the occurrence of olivine (in association with antigorite and brucite)  
588 and dolomite decomposition within magnetite (Fig. 3B–D), suggest that the  
589 studied ophidolomites may have acted as a possible H<sub>2</sub> source for the reduction  
590 process. Alternatively, the reduced fluids may be externally derived from the  
591 rehydration of surrounding serpentinites, which contain ~25 vol% metamorphic  
592 olivine (Shen et al., 2015). Moreover, the elevated <sup>87</sup>Sr/<sup>86</sup>Sr ratios of calcite,  
593 decoupled from dolomite but in general agreement with the Tianshan serpentinites  
594 that have largely inherited Sr isotope values of the seawater (Fig. 6A; Peng et al.,  
595 2020), likely reflect Sr isotope exchange with the serpentinizing fluids during  
596 dolomite reduction.

597 In the studied rocks, a majority of dolomite-hosted fluid inclusions form  
598 trails crosscutting grain boundaries (Fig. 4A–D), indicating that they were trapped  
599 along fractures of dolomite and preserved through subsequent healing of these  
600 fractures. The relative timing of fluid entrapment can be obtained by fluid  
601 inclusion isochores intersecting the retrograde path of the Chinese southwestern  
602 Tianshan (Tan et al., 2017), which constrained *P–T* conditions of about 1–3 kbar  
603 and 250–350 °C (Fig. 8). The *P–T* constraints, lower than 7–9 kbar and 410–430  
604 °C, suggest that entrapment of the fluid inclusions postdates the onset of dolomite  
605 reduction (Fig. 8). Based on the localized alteration of dolomite (Fig. 2), we infer  
606 that the reactive reduced fluids may be limited and have been largely consumed  
607 by dolomite after the reduction started, leading to the stability of relict reactants

608 until the fractures were generated to provide fluid pathways and subsequently  
609 healed to preserve the fluid inclusions. This is in agreement with our petrographic  
610 observations that dolomite-hosted fluid inclusions are nearly devoid of calcite and  
611 brucite daughter minerals representative of dolomite reduction within the  
612 inclusions (Section 4.2). Given that the retrograde serpentinization responsible for  
613 dolomite reduction could propagate to relatively lower  $P$ – $T$  conditions (e.g., 2–10  
614 kbar and 250–350 °C; Li et al., 2007, 2010), the possibility may exist that the  
615 timing of fluid inclusion trapping is slightly later than or close to that of abiotic  
616  $\text{CH}_4$  formation. Under this circumstance, the reduction process of dolomite  
617 probably came to a halt due to the exhaustion of the reactive reduced fluids (see  
618 above), closely followed by fluid entrapment along the fractures. Note that this  
619 possibility depends primarily on  $P$ – $T$  conditions for the propagation of the  
620 retrograde serpentinization, which, however, remain uncertain despite the  
621 calculations by Li et al. (2007, 2010) based on a few reactions observed in  
622 serpentinites and associated rodingites. Uncertainties may mainly derive from the  
623 controversial  $P$ – $T$  conditions for the transformation of chrysotile into antigorite  
624 (Evans et al., 1976; Scambelluri et al., 2004; Li et al., 2007, 2010) and the  
625 ignorance of several potential reactions (e.g., the lizardite to antigorite transition;  
626 Guillot et al., 2015) in rocks for the constraints (Fig. 8).

### 627 **5.3. Implications for C mobility in subduction zones**

628 Laboratory studies demonstrated that carbonate aqueous reduction at  $f\text{O}_2$  far  
629 below the FMQ buffer (e.g., the IM or iron–wüstite (IW) buffer) under HP

630 conditions is a potential pathway for significant production of abiotic CH<sub>4</sub> in  
631 subduction zones (Lazar et al., 2014; Mukhina et al., 2017). Moreover, field-based  
632 investigations constrained a relatively wide range of log  $fO_2$  values for HP abiotic  
633 formation of CH<sub>4</sub> via carbonate reduction in ophicalcites from the Western Alps  
634 ( $\Delta FMQ$   $-6.0 \sim -3.0$  at 1 GPa and 400 °C; Vitale Brovarone et al., 2017) and in  
635 carbonated eclogites from the Tianshan ( $\Delta FMQ$   $-2.5$  at 2.5 GPa and 550 °C; Tao  
636 et al., 2018a). In the present study, thermodynamic simulations suggest that  
637 abiotic CH<sub>4</sub> generation through dolomite aqueous reduction can occur at  $fO_2$   
638 slightly lower than or even close to the FMQ buffer (Fig. 7A). The stability of  
639 CH<sub>4</sub>-bearing fluids at FMQ conditions is reflected by a three-dimensional  $P$ - $T$ -  
640 log  $fO_2$  diagram calculated for graphite/diamond-saturated COH fluids (Tumiati  
641 and Malaspina, 2019), displaying that the FMQ surface is below the maximum  
642 H<sub>2</sub>O activity surface where CH<sub>4</sub> is the dominant C-bearing species under the  
643 studied  $P$ - $T$  conditions. Furthermore, experiments conducted on HP aqueous  
644 reduction of organic matter demonstrated that CH<sub>4</sub>-bearing fluids in equilibrium  
645 with graphite can stabilize at  $fO_2$  approaching the FMQ buffer (i.e., the Co-CoO  
646 or Ni-NiO buffer at 2.5 GPa and 600–700 °C; Li, 2017). In the studied samples,  
647 however, graphite was sporadically detected in the cloudy calcite-brucite  
648 intergrowths (Supplementary Fig. S7), which may be attributed to the high  $fH_2$   
649 conditions (see below).

650 Graphite has been observed in several CH<sub>4</sub>-absent (Malvoisin et al., 2012;  
651 Galvez et al., 2013a, b; Zhu et al., 2020) or CH<sub>4</sub>-bearing (Vitale Brovarone et al.,

652 [2017, 2020; Tao et al., 2018a](#)) lithologies in subduction zones, formed by  
653 carbonate anhydrous graphitization or precipitating from the reduced COH fluids.  
654 Compared with carbonate minerals (e.g., [Kelemen and Manning, 2015](#)), graphite  
655 represents a relatively stable phase that may transfer subducted C into the deep  
656 Earth ([Galvez et al., 2013a; Duncan and Dasgupta, 2017; Eguchi et al., 2020](#)),  
657 while recent studies suggest that graphite could be partly dissolved in subduction-  
658 zone fluids ([Tumiati et al., 2017, 2020](#) and references therein). In our study,  
659 however, the widespread occurrence of CH<sub>4</sub> compared to graphite illustrates that  
660 the equilibrium between graphite and CH<sub>4</sub> may be largely controlled by  $fH_2$  ([Fig.](#)  
661 [7A](#)), implying that an increase in  $fH_2$  would contribute to the transformation of  
662 graphite into CH<sub>4</sub> at convergent plate boundaries. This is in accord with the  
663 microstructure-based recognition of an additional abiotic CH<sub>4</sub>-forming event in  
664 reduced ophicalcites from the Western Alps, attributed to H<sub>2</sub>-induced reduction  
665 of the newly formed graphite during ascent of the slab ([Vitale Brovarone et al.,](#)  
666 [2017](#)). Moreover, experiments performed on the hydrogenation of graphite at high  
667  $P$ - $T$  conditions (5.0–5.5 GPa and >1500 °C) yielded considerable CH<sub>4</sub>, indicating  
668 that  $fH_2$  may play an important role in governing abiotic CH<sub>4</sub> genesis in deep  
669 subduction zones ([Sharma et al., 2009](#)). Indeed, graphite has a very low content  
670 or nearly absent in several CH<sub>4</sub>-H<sub>2</sub>-bearing serpentinites in subduction zones  
671 ([Peretti et al., 1992; Vitale Brovarone et al., 2020](#)), in agreement with the CH<sub>4</sub>-  
672 H<sub>2</sub>-H<sub>2</sub>O equilibrated region below the graphite saturation curve predicted by the  
673 isobaric–isothermal C–O–H diagram (e.g., [Holloway, 1984](#)).

674 While the reduction in our study happened during exhumation of the slab,  
675 the proposed  $P$ – $T$  estimates are similar to those of carbonate reduction during  
676 shallow subduction in comparable metamorphic settings (Malvoisin et al., 2012;  
677 Galvez et al., 2013a, b; Vitale Brovarone et al., 2017; Giuntoli et al., 2020), which  
678 are in general accord with the prograde  $P$ – $T$  paths of subduction zones predicted  
679 by thermal models (Syracuse et al., 2010) and metamorphic rocks (Penniston-  
680 Dorland et al., 2015) (Fig. 9A). Thus, the reduction process of dolomite described  
681 here may have implications for subducted C mobility. Laboratory experiments  
682 and field observations provide evidence for dolomite formation through mineral  
683 carbonation in subseafloor serpentinization systems (Grozeva et al., 2017),  
684 suggesting that subduction of these hydrothermally altered oceanic rocks  
685 represents a potential dolomite source in downgoing slabs. Indeed, dolomite,  
686 despite its variable contents (ca. 5–50 vol%), is not uncommon in several slab-  
687 and mantle wedge-forming lithologies including metaultramafic, metamafic, and  
688 metasedimentary rocks (e.g., Li et al., 2012, 2014; Tao et al., 2014, 2018b; Falk  
689 and Kelemen, 2015; Zhu et al., 2018). Furthermore, mounting field evidence, as  
690 well as thermodynamic modelling, suggests that serpentinization of ultramafic  
691 rocks can happen at relatively shallow depths (ca. 20–30 km) in subducted slabs,  
692 or even up to ca. 70–80 km (Li et al., 2007, 2010; Vitale Brovarone et al., 2017,  
693 2020; Lazar, 2020). Therefore, an infiltration of these serpentinization-derived  
694 reduced fluids would be conducive to dolomite reduction and abiotic CH<sub>4</sub>  
695 generation during shallow subduction, which may represent a feasible mechanism



696 for the mobility of subducted C (Fig. 9B). Moreover, release of such deep-sourced  
697 reduced fluids might support the hypothesis that subduction zones potentially  
698 provide energy to sustain subsurface chemosynthetic microbial life at habitable  
699 temperatures in the overlying forearc (e.g., Curtis et al., 2013; Plümper et al., 2017;  
700 Fryer et al., 2020; Lazar, 2020; Vitale Brovarone et al., 2020; Wheat et al., 2020).  
701 However, uncertainties remain regarding the implications presented here,  
702 particularly under circumstances where the scale and extent of dolomite reduction  
703 are insufficiently quantified.

704

## 705 **6. CONCLUSIONS**

706 Reduction of ophidolomites in the Chinese southwestern Tianshan *HP–UHP*  
707 metamorphic belt provides new insights into abiotic CH<sub>4</sub> generation in subduction  
708 zones. Petrological characteristics, Raman spectroscopic and microthermometric  
709 data of fluid inclusions, Sr and C isotope compositions, and thermodynamic  
710 results demonstrate dolomite reduction into the phase assemblage of calcite +  
711 brucite + CH<sub>4</sub>, likely related to retrograde serpentinization starting at 7–9 kbar  
712 and 410–430 °C in the subduction zone. The onset of dolomite reduction is prior  
713 to fluid entrapment that happened at about 1–3 kbar and 250–350 °C, leading to  
714 the widespread distribution of secondary fluid inclusions along healed fractures  
715 of dolomite. Model calculations suggest that an infiltration of H<sub>2</sub>O-rich fluids at  
716 relatively high  $fH_2$  (e.g.,  $y_{H_2O} = 0.999995$  at  $\log fH_2 = 0.8$ ) can contribute to this  
717 reduction process, but the possibility of carbonate methanation by H<sub>2</sub>-rich fluids

718 cannot be excluded. The abundant CH<sub>4</sub>-bearing fluid inclusions in these rocks  
719 indicate that  $fH_2$  probably plays an important role in regulating the speciation of  
720 subducted C, implying that an increase in  $fH_2$  may accelerate abiotic formation of  
721 CH<sub>4</sub> through dolomite reduction at convergent plate boundaries. Thus, alteration  
722 of dolomite-bearing lithologies represents a potential mechanism for abiotic  
723 synthesis of CH<sub>4</sub> in subduction zones, which may have implications for the  
724 mobility of subducted C.

725

## 726 **ACKNOWLEDGEMENTS**

727 This work was funded by the National Key Research and Development  
728 Program of China (No. 2019YFA0708501), the National Natural Science  
729 Foundation of China (No. 41520104004), and the Scientific Research Foundation  
730 of Pilot National Laboratory for Marine Science and Technology (Qingdao) (No.  
731 JCZX202011). Simone Tumiati acknowledges support from the Italian program  
732 MIUR PRIN (No. 2017ZE49E7\_002). Alberto Vitale Brovarone was supported  
733 by the ERC CoG “DeepSeep” (No. 864045), an ANR T-ERC grant (No. LS  
734 171301), and a MIUR Levi Montalcini grant; by the Deep Carbon Observatory  
735 (DCO) Deep Energy community; and by the Richard Lounsbery foundation.  
736 Discussions with James Connolly, Thomas Bader, Wen Zhang, Yueheng Yang,  
737 Enrico Cannà, Ryosuke Oyanagi, Xiaoxia Li, Xia Zhang, and Shujie Wang are  
738 highly appreciated. We thank Yang Wang and Zhicheng Liu for their help during  
739 fieldwork, and Hongrui Ding, Liangliang Huang, Hongwei Li, Xiangtian Jin, Nan

740 Li, Xiaoli Li, and Jiangqing Liu for their patient assistance during sample analyses.  
741 The authors are grateful to anonymous reviewers (three for a very early draft and  
742 three for a more recent draft) for their detailed and constructive comments and to  
743 Frieder Klein (Associate Editor) for his careful editorial handling and helpful  
744 suggestions.

745

## 746 **APPENDIX A. SUPPLEMENTARY MATERIAL**

747 Supplementary data to this article can be found online at <https://doi.org/XXXX>.

748

## 749 **RESEARCH DATA**

750 All research data used in this study are included in tables and the appendix file.

751

## 752 **REFERENCES**

753 Ague J. J. and Nicolescu S. (2014) Carbon dioxide released from subduction  
754 zones by fluid-mediated reactions. *Nat. Geosci.* **7**, 355–360.

755 Alt J. C., Garrido C. J., Shanks W. C., Turchyn A., Padrón-Navarta J. A., López  
756 Sánchez-Vizcaíno V., Gómez-Pugnaire M. T. and Marchesi C. (2012)  
757 Recycling of water, carbon, and sulfur during subduction of serpentinites: a  
758 stable isotope study of Cerro del Almirez, Spain. *Earth Planet. Sci. Lett.* **327–**  
759 **328**, 50–60.

760 Alt J. C., Schwarzenbach E. M., Früh-Green G. L., Shanks W. C., Bernasconi S.  
761 M., Garrido C. J., Crispini L., Gaggero L., Padrón-Navarta J. A. and Marchesi  
762 C. (2013) The role of serpentinites in cycling of carbon and sulfur: seafloor  
763 serpentinitization and subduction metamorphism. *Lithos* **178**, 40–54.

- 764 Angiboust S., Pettke T., De Hoog J. C. M., Caron B. and Oncken O. (2014)  
765 Channelized fluid flow and eclogite-facies metasomatism along the  
766 subduction shear zone. *J. Petrol.* **55**, 883–916.
- 767 Arai S., Ishimaru S. and Mizukami T. (2012) Methane and propane micro-  
768 inclusions in olivine in titanoclinohumite-bearing dunites from the Sanbagawa  
769 high-P metamorphic belt, Japan: Hydrocarbon activity in a subduction zone  
770 and Ti mobility. *Earth Planet. Sci. Lett.* **353**, 1–11.
- 771 Aranovich L. Y. and Newton R. C. (1996) H<sub>2</sub>O activity in concentrated NaCl  
772 solutions at high pressures and temperatures measured by the brucite–  
773 periclase equilibrium. *Contrib. Mineral. Petrol.* **125**, 200–212.
- 774 Berg G. W. (1986) Evidence for carbonate in the mantle. *Nature* **324**, 50–51.
- 775 Bodnar R. J. (2003) Reequilibration of fluid inclusions. In *Fluid Inclusions:*  
776 *Analysis and Interpretation* (eds. I. Samson, A. Anderson and D. Marshall).  
777 Mineral Association of Canada, Short Course 32. pp. 213–230.
- 778 Bonatti E., Emiliani C., Ferrera G., Honnorez J. and Rydell H. (1974) Ultramafic-  
779 carbonate breccias from the equatorial Mid Atlantic Ridge. *Mar. Geol.* **16**,  
780 83–102.
- 781 Bottinga Y. (1969) Calculated fractionation factors for carbon and hydrogen  
782 isotope exchange in the system calcite–carbon dioxide–graphite–methane–  
783 hydrogen–water vapor. *Geochim. Cosmochim. Acta* **33**, 49–64.
- 784 Boutier A., Vitale Brovarone A., Martinez I., Sissmann O. and Mana S. (2021)  
785 High-pressure serpentinization and abiotic methane formation in  
786 metaperidotite from the Appalachian subduction, northern Vermont. *Lithos*  
787 **396–397**, 106190.
- 788 Cannà E., Scambelluri M., Bebout G. E., Agostini S., Pettke T., Godard M. and  
789 Crispini L. (2020) Ophicarbonates evolution from seafloor to subduction and  
790 implications for deep-Earth C cycling. *Chem. Geol.* **546**, 119626.

791 Charlou J. L., Donval J. P., Fouquet Y., Jean-Baptiste P. and Holm N. (2002)  
792 Geochemistry of high H<sub>2</sub> and CH<sub>4</sub> vent fluids issuing from ultramafic rocks at  
793 the Rainbow hydrothermal field (36°14'N, MAR). *Chem. Geol.* **191**, 345–359.

794 Charlou J. L., Donval J. P., Konn C., Ondréas H., Fouquet Y., Jean-Baptiste P.  
795 and Fourré E. (2010) High production and fluxes of H<sub>2</sub> and CH<sub>4</sub> and evidence  
796 of abiotic hydrocarbon synthesis by serpentinization in ultramafic-hosted  
797 hydrothermal systems on the Mid-Atlantic Ridge. In *Diversity of*  
798 *Hydrothermal Systems on Slow Spreading Ocean Ridges* (eds. P. A. Rona, C.  
799 W. Devey, J. Dymont and B. J. Murton). American Geophysical Union,  
800 Washington, DC. pp. 265–296.

801 Clerc C., Boulvais P., Lagabrielle Y. and de Saint Blanquat M. (2014)  
802 Ophicalcites from the northern Pyrenean belt: a field, petrographic and stable  
803 isotope study. *Int. J. Earth Sci.* **103**, 141–163.

804 Collins N. C., Bebout G. E., Angiboust S., Agard P., Scambelluri M., Crispini L.  
805 and John T. (2015) Subduction zone metamorphic pathway for deep carbon  
806 cycling: II. Evidence from HP/UHP metabasaltic rocks and ophicarbonates.  
807 *Chem. Geol.* **412**, 132–150.

808 Connolly J. A. D. (1995) Phase diagram methods for graphitic rocks and  
809 application to the system C–O–H–FeO–TiO<sub>2</sub>–SiO<sub>2</sub>. *Contrib. Mineral. Petrol.*  
810 **119**, 94–116.

811 Connolly J. A. D. (2005) Computation of phase equilibria by linear programming:  
812 A tool for geodynamic modeling and its application to subduction zone  
813 decarbonation. *Earth Planet. Sci. Lett.* **236**, 524–541.

814 Connolly J. A. D. and Galvez M. E. (2018) Electrolytic fluid speciation by Gibbs  
815 energy minimization and implications for subduction zone mass transfer.  
816 *Earth Planet. Sci. Lett.* **501**, 90–102.

817 Consuma G., Braga R., Giovanardi T., Bersani D., Konzett J., Lugli F.,  
818 Mazzucchelli M. and Tropper P. (2020) *In situ* Sr isotope analysis of mantle

819 carbonates: Constraints on the evolution and sources of metasomatic carbon-  
820 bearing fluids in a paleo-collisional setting. *Lithos* **354–355**, 105334.

821 Curtis A. C., Wheat C. G., Fryer P. and Moyer C. L. (2013) Mariana forearc  
822 serpentinite mud volcanoes harbor novel communities of extremophilic  
823 *Archaea*. *Geomicrobiol. J.* **30**, 430–441.

824 Dasgupta R. and Hirschmann M. M. (2010) The deep carbon cycle and melting  
825 in Earth's interior. *Earth Planet. Sci. Lett.* **298**, 1–13.

826 Duncan M. S. and Dasgupta R. (2017) Rise of Earth's atmospheric oxygen  
827 controlled by efficient subduction of organic carbon. *Nat. Geosci.* **10**, 387–  
828 392.

829 Eguchi J., Seales J. and Dasgupta R. (2020) Great Oxidation and Lomagundi  
830 events linked by deep cycling and enhanced degassing of carbon. *Nat. Geosci.*  
831 **13**, 71–76.

832 Etiope G. and Schoell M. (2014) Abiotic gas: Atypical, but not rare. *Elements* **10**,  
833 291–296.

834 Etiope G. and Sherwood Lollar B. (2013) Abiotic Methane on Earth. *Rev.*  
835 *Geophys.* **51**, 276–299.

836 Etiope G., Schoell M. and Hosgörmez H. (2011) Abiotic methane flux from the  
837 Chimaera seep and Tekirova ophiolites (Turkey): Understanding gas  
838 exhalation from low temperature serpentinization and implications for Mars.  
839 *Earth Planet. Sci. Lett.* **310**, 96–104.

840 Evans B. W. (2010) Lizardite versus antigorite serpentinite: Magnetite, hydrogen,  
841 and life(?). *Geology* **38**, 879–882.

842 Evans K. A. (2012) The redox budget of subduction zones. *Earth Sci. Rev.* **113**,  
843 11–32.

844 Evans B. W., Johannes W., Oterdoom H. and Trommsdorff V. (1976) Stability of  
845 chrysotile and antigorite in the serpentine multisystem. *Schweiz. Mineral.*  
846 *Petrogr. Mitt.* **56**, 79–93.

847 Facq S., Daniel I., Montagnac G., Cardon H. and Sverjensky D. A. (2014) *In situ*  
848 Raman study and thermodynamic model of aqueous carbonate speciation in  
849 equilibrium with aragonite under subduction zone conditions. *Geochim.*  
850 *Cosmochim. Acta* **132**, 375–390.

851 Falk E. S. and Kelemen P. B. (2015) Geochemistry and petrology of listvenite in  
852 the Samail ophiolite, Sultanate of Oman: Complete carbonation of peridotite  
853 during ophiolite emplacement. *Geochim. Cosmochim. Acta* **160**, 70–90.

854 Förster B., Braga R., Aulbach S., Lo Pò D., Bargossi G. M. and Mair V. (2017)  
855 A petrographic study of carbonate phases in the Ulten Zone ultramafic rocks:  
856 Insights into carbonation in the mantle wedge and exhumation-related  
857 decarbonation. *Ophioliti* **42**, 105–127.

858 Frezzotti M. L., Selverstone J., Sharp Z. D. and Compagnoni R. (2011) Carbonate  
859 dissolution during subduction revealed by diamond-bearing rocks from the  
860 Alps. *Nat. Geosci.* **4**, 703–706.

861 Früh-Green G. L., Kelley D. S., Bernasconi S. M., Karson J. A., Ludwig K. A.,  
862 Butterfield D. A., Boschi C. and Proskurowski G. (2003) 30000 years of  
863 hydrothermal activity at the Lost City vent field. *Nature* **301**, 495–498.

864 Fryer P., Wheat C. G., Williams T., Kelley C., Johnson K., Ryan J., Kurz W.,  
865 Shervais J., Albers E., Bekins B., Debret B., Deng J., Dong Y., Eickenbusch  
866 P., Frery E., Ichiyama Y., Johnston R., Kevorkian R., Magalhaes V.,  
867 Mantovanelli S., Menapace W., Menzies C., Michibayashi K., Moyer C.,  
868 Mullane K., Park J.-W., Price R., Sissmann O., Suzuki S., Takai K., Walter  
869 B., Zhang R., Amon D., Glickson D. and Pomponi S. (2020) Mariana  
870 serpentinite mud volcanism exhumes subducted seamount materials:  
871 implications for the origin of life. *Phil. Trans. R. Soc. A* **378**, 20180425.

872 Fukui H., Ohtaka O., Fujisawa T., Kunisada T., Suzuki T. and Kikegawa T. (2003)  
873 Thermo-elastic property of Ca(OH)<sub>2</sub> portlandite. *High Pressure Res.* **23**, 55–  
874 61.

875 Galvez M. E. and Pubellier M. (2019) How do subduction zones regulate the  
876 carbon cycle? In *Deep carbon: Past to Present* (eds. B. N. Orcutt, I. Daniel  
877 and R. Dasgupta). Cambridge University Press, Cambridge. pp. 276–312.

878 Galvez M. E., Beyssac O., Martinez I., Benzerara K., Chaduteau C., Malvoisin B.  
879 and Malavieille J. (2013a) Graphite formation by carbonate reduction during  
880 subduction. *Nat. Geosci.* **6**, 473–477.

881 Galvez M. E., Martinez I., Beyssac O., Benzerara K., Agrinier P. and Assayag N.  
882 (2013b) Metasomatism and graphite formation at a lithological interface in  
883 Malaspina (Alpine Corsica, France). *Contrib. Mineral. Petrol.* **166**, 1687–  
884 1708.

885 Giuntoli F., Vitale Brovarone A. and Menegon L. (2020) Feedback between high-  
886 pressure genesis of abiotic methane and strain localization in subducted  
887 carbonate rocks. *Sci. Rep.* **10**, 9848.

888 Goldstein R. H. and Reynolds T. J. (1994) *Systematics of fluid inclusions in*  
889 *diagenetic minerals*. SEPM (Society for Sedimentary Geology) Short Course  
890 31, Tulsa.

891 Grozeva N. G., Klein F., Seewald J. S. and Sylva S. P. (2017) Experimental study  
892 of carbonate formation in oceanic peridotite. *Geochim. Cosmochim. Acta* **199**,  
893 264–286.

894 Grozeva N. G., Klein F., Seewald J. S. and Sylva S. P. (2020) Chemical and  
895 isotopic analyses of hydrocarbon-bearing fluid inclusions in olivine-rich rocks.  
896 *Phil. Trans. R. Soc. A* **378**, 20180431.

897 Guillot S., Schwartz S., Reynard B., Agard P. and Prigent C. (2015) Tectonic  
898 significance of serpentinites. *Tectonophysics* **646**, 1–19.

899 Hayes J. M. and Waldbauer J. R. (2006) The carbon cycle and associated redox  
900 processes through time. *Phil. Trans. R. Soc. B* **361**, 931–950.

901 Hoefs J. (2009) *Stable Isotope Geochemistry, 6th ed.* Springer-Verlag, Berlin  
902 Heidelberg.



903 Holland T. J. B. and Powell R. (1998) An internally consistent thermodynamic  
904 data set for phases of petrological interest. *J. Metamorph. Geol.* **16**, 309–343.

905 Holloway J. R. (1984) Graphite–CH<sub>4</sub>–H<sub>2</sub>O–CO<sub>2</sub> equilibria at low-grade  
906 metamorphic conditions. *Geology* **12**, 455–458.

907 Hu Z., Liu Y., Gao S., Xiao S., Zhao L., Günther D., Li M., Zhang W. and Zong  
908 K. (2012) A “wire” signal smoothing device for laser ablation inductively  
909 coupled plasma mass spectrometry analysis. *Spectrochim. Acta B* **78**, 50–57.

910 Hu H., Vitale Brovarone A., Zhang L., Piccoli F., Peng W. and Shen T. (2021)  
911 Retrograde carbon sequestration in orogenic complexes: A case study from  
912 the Chinese southwestern Tianshan. *Lithos* **392–393**, 106151.

913 Huang F., Daniel I., Cardon H., Montagnac G. and Sverjensky D. A. (2017)  
914 Immiscible hydrocarbon fluids in the deep carbon cycle. *Nat. Commun.* **8**,  
915 15798.

916 Jaeckel K., Bebout G. E. and Angiboust S. (2018) Deformation-enhanced fluid  
917 and mass transfer along Western and Central Alps paleo-subduction interfaces:  
918 Significance for carbon cycling models. *Geosphere* **14**, 2355–2375.

919 Johannes W. and Puhan D. (1971) The calcite-aragonite transition, reinvestigated.  
920 *Contrib. Mineral. Petrol.* **31**, 28–38.

921 Kelemen P. B. and Manning C. E. (2015) Reevaluating carbon fluxes in  
922 subduction zones, what goes down, mostly comes up. *Proc. Natl. Acad. Sci.*  
923 *USA* **112**, E3997–E4006.

924 Kelley D. S., Karson J. A., Blackman D. K., Früh-Green G. L., Butterfield D. A.,  
925 Lilley M. D., Olson E. J., Schrenk M. O., Roe K. K., Lebon G. T., Rivizzigno  
926 P. and the AT3-60 Shipboard Party. (2001) An off-axis hydrothermal vent  
927 field near the Mid-Atlantic Ridge at 30° N. *Nature* **412**, 145–149.

928 Kelley D. S., Karson J. A., Früh-Green G. L., Yoerger D. R., Shank T. M.,  
929 Butterfield D. A., Hayes J. M., Schrenk M. O., Olson E. J., Proskurowski G.,  
930 Jakuba M., Bradley A., Larson B., Ludwig K., Glickson D., Buckman K.,  
931 Bradley A. S., Brazelton W. J., Roe K., Elend M. J., Delacour A., Bernasconi

- 932 S. M., Lilley M. D., Baross J. A., Summons R. E. and Sylva S. P. (2005) A  
933 serpentinite-hosted ecosystem: The Lost City hydrothermal field. *Science* **307**,  
934 1428–1434.
- 935 Klein F., Bach W. and McCollom T. M. (2013) Compositional controls on  
936 hydrogen generation during serpentinization of ultramafic rocks. *Lithos* **178**,  
937 55–69.
- 938 Klein F., Humphris S. E., Guo W., Schubotz F., Schwarzenbach E. M. and Orsi  
939 W. D. (2015) Fluid mixing and the deep biosphere of a fossil Lost City-type  
940 hydrothermal system at the Iberia Margin. *Proc. Natl. Acad. Sci. USA* **112**,  
941 12036–12041.
- 942 Klein F., Grozeva N. G. and Seewald J. S. (2019) Abiotic methane synthesis and  
943 serpentinization in olivine-hosted fluid inclusions. *Proc. Natl. Acad. Sci. USA*  
944 **116**, 17666–17672.
- 945 Klein F., Tarnas J. D. and Bach W. (2020) Abiotic sources of molecular hydrogen  
946 on Earth. *Elements* **16**, 19–24.
- 947 Lafay R., Baumgartner L. P., Stephane S., Suzanne P., German M. H. and Torsten  
948 V. (2017) Petrologic and stable isotopic studies of a fossil hydrothermal  
949 system in ultramafic environment (Chenaillet ophicalcites, Western Alps,  
950 France): Processes of carbonate cementation. *Lithos* **294–295**, 319–338.
- 951 Lamadrid H. M., Rimstidt J. D., Schwarzenbach E. M., Klein F., Ulrich S.,  
952 Dolocan A. and Bodnar R. J. (2017) Effect of water activity on rates of  
953 serpentinization of olivine. *Nat. Commun.* **8**, 16107.
- 954 Lamadrid H. M., Zajacz Z., Klein F. and Bodnar R. J. (2021) Synthetic fluid  
955 inclusions XXIII. Effect of temperature and fluid composition on rates of  
956 serpentinization of olivine. *Geochim. Cosmochim. Acta* **292**, 285–308.
- 957 Lazar C. (2020) Using silica activity to model redox-dependent fluid  
958 compositions in serpentinites from 100 to 700 °C and from 1 to 20 kbar. *J.*  
959 *Petrol.* **61**, ega101.

- 960 Lazar C., Zhang C., Manning C. E. and Mysen B. O. (2014) Redox effects on  
961 calcite–portlandite–fluid equilibria at forearc conditions: Carbon mobility,  
962 methanogenesis, and reduction melting of calcite. *Am. Mineral.* **99**, 1604–  
963 1615.
- 964 Li Y. (2017) Immiscible C–H–O fluids formed at subduction zone conditions.  
965 *Geochem. Perspect. Lett.* **3**, 12–21.
- 966 Li X.-P., Zhang L., Wei C., Ai Y. and Chen J. (2007) Petrology of rodingite  
967 derived from eclogite in western Tianshan, China. *J. Metamorph. Geol.* **25**,  
968 363–382.
- 969 Li X.-P., Zhang L.-F., Wilde S. A., Song B. and Liu X.-M. (2010) Zircons from  
970 rodingite in the Western Tianshan serpentinite complex: mineral chemistry  
971 and U–Pb ages define nature and timing of rodingitization. *Lithos* **118**, 17–34.
- 972 Li J.-L., Klemd R., Gao J. and Meyer M. (2012) Coexisting carbonate-bearing  
973 eclogite and blueschist in SW Tianshan, China: Petrology and phase equilibria.  
974 *J. Asian Earth Sci.* **60**, 174–187.
- 975 Li J.-L., Klemd R., Gao J. and Meyer M. (2014) Compositional zoning in  
976 dolomite from lawsonite-bearing eclogite (SW Tianshan, China): Evidence  
977 for prograde metamorphism during subduction of oceanic crust. *Am. Mineral.*  
978 **99**, 206–217.
- 979 Li X., Zhang L., Wei C., Slabunov A. I. and Bader T. (2018) Quartz and  
980 orthopyroxene exsolution lamellae in clinopyroxene and the metamorphic *P*–  
981 *T* path of Belomorian eclogites. *J. Metamorph. Geol.* **36**, 1–22.
- 982 Lin F., Bodnar R. J. and Becker S. P. (2007) Experimental determination of the  
983 Raman CH<sub>4</sub> symmetric stretching ( $\gamma_1$ ) band position from 1–650 bar and 0.3–  
984 22 °C: Application to fluid inclusion studies. *Geochim. Cosmochim. Acta* **71**,  
985 3746–3756.
- 986 Lin M., Zhang G., Li N., Li H. and Wang J. (2021) An improved *in situ* zircon  
987 U–Pb dating method at high spatial resolution ( $\leq 10 \mu\text{m}$  spot) by LA-MC-  
988 ICP-MS and its application. *Geostand. Geoanal. Res.* **45**, 265–285.

- 989 Liou J. G., Tsujimori T., Zhang R. Y., Katayama I. and Maruyama S. (2004)  
990 Global UHP metamorphism and continental subduction/collision: the  
991 Himalayan model. *Int. Geol. Rev.* **46**, 1–27.
- 992 Lü Z. and Zhang L. (2012) Coesite in the eclogite and schist of the Atantayi Valley,  
993 southwestern Tianshan, China. *Chinese Sci. Bull.* **57**, 1467–1472.
- 994 Lü Z., Bucher K., Zhang L. and Du J. (2012a) The Habutengsu metapelites and  
995 metagreywackes in western Tianshan, China: metamorphic evolution and  
996 tectonic implications. *J. Metamorph. Geol.* **30**, 907–926.
- 997 Lü Z., Zhang L., Du J., Yang X., Tian Z. and Xia B. (2012b) Petrology of HP  
998 metamorphic veins in coesite-bearing eclogite from western Tianshan, China:  
999 Fluid processes and elemental mobility during exhumation in a cold  
1000 subduction zone. *Lithos* **136–139**, 168–186.
- 1001 Malvoisin B., Chopin C., Brunet F. and Galvez M. E. (2012) Low-temperature  
1002 wollastonite formed by carbonate reduction: a marker of serpentinite redox  
1003 conditions. *J. Petrol.* **53**, 159–176.
- 1004 McCollom T. M. and Bach W. (2009) Thermodynamic constraints on hydrogen  
1005 generation during serpentinization of ultramafic rocks. *Geochim. Cosmochim.*  
1006 *Acta* **73**, 856–875.
- 1007 McCollom T. M. and Seewald J. S. (2001) A reassessment of the potential for  
1008 reduction of dissolved CO<sub>2</sub> to hydrocarbons during serpentinization of olivine.  
1009 *Geochim. Cosmochim. Acta* **65**, 3769–3778.
- 1010 McCollom T. M. and Seewald J. S. (2013) Serpentinites, hydrogen, and life.  
1011 *Elements* **9**, 129–134.
- 1012 McDermott J. M., Seewald J. S., German C. R. and Sylva S. P. (2015) Pathways  
1013 for abiotic organic synthesis at submarine hydrothermal fields. *Proc. Natl.*  
1014 *Acad. Sci. USA* **112**, 7668–7672.
- 1015 Ménez B. (2020) Abiotic hydrogen and methane: Flues for life. *Elements* **16**, 39–  
1016 46.

- 1017 Mukhina E., Kolesnikov A. and Kutcherov V. (2017) The lower pT limit of deep  
1018 hydrocarbon synthesis by CaCO<sub>3</sub> aqueous reduction. *Sci. Rep.* **7**, 5749.
- 1019 Peng W., Zhang L., Shen T. and Hu H. (2018) Implications for the deep carbon  
1020 cycle from the carbonation in subduction zones: A case study of carbonated  
1021 micaschists from Chinese southwestern Tianshan. *Acta Petrol. Sin.* **34**, 1204–  
1022 1218.
- 1023 Peng W., Zhang L., Menzel M. D., Vitale Brovarone A., Tumiati S., Shen T. and  
1024 Hu H. (2020) Multistage CO<sub>2</sub> sequestration in the subduction zone: Insights  
1025 from exhumed carbonated serpentinites, SW Tianshan UHP belt, China.  
1026 *Geochim. Cosmochim. Acta* **270**, 218–243.
- 1027 Penniston-Dorland S. C., Kohn M. J. and Manning C. E. (2015) The global range  
1028 of subduction zone thermal structures from exhumed blueschists and eclogites:  
1029 Rocks are hotter than models. *Earth Planet. Sci. Lett.* **428**, 243–254.
- 1030 Peretti A., Dubessy J., Mullis J., Frost B. R. and Trommsdorff V. (1992) Highly  
1031 reducing conditions during Alpine metamorphism of the Malenco peridotite  
1032 (Sondrio, northern Italy) indicated by mineral paragenesis and H<sub>2</sub> in fluid  
1033 inclusions. *Contrib. Mineral. Petrol.* **112**, 329–340.
- 1034 Piccoli F., Vitale Brovarone A., Beyssac O., Martinez I., Ague J. J. and Chaduteau  
1035 C. (2016) Carbonation by fluid–rock interactions at high-pressure conditions:  
1036 Implications for carbon cycling in subduction zones. *Earth Planet. Sci. Lett.*  
1037 **445**, 146–159.
- 1038 Piccoli F., Vitale Brovarone A. and Ague J. J. (2018) Field and petrological study  
1039 of metasomatism and high-pressure carbonation from lawsonite eclogite-  
1040 facies terrains, Alpine Corsica. *Lithos* **304–307**, 16–37.
- 1041 Plümper O., King H. E., Geisler T., Liu Y., Pabst S., Savov I. P., Rost D. and Zack  
1042 T. (2017) Subduction zone forearc serpentinites as incubators for deep  
1043 microbial life. *Proc. Natl. Acad. Sci. USA* **114**, 4324–4329.

- 1044 Proskurowski G., Lilley M. D., Seewald J. S., Früh-Green, G. L., Olson, E. J.,  
1045 Lupton, J. E., Sylva, S. P. and Kelley, D. S. (2008) Abiogenic hydrocarbon  
1046 production at Lost City hydrothermal field. *Science* **319**, 604–607.
- 1047 Ramos F. C., Wolff J. A. and Tollstrup D. L. (2004) Measuring  $^{87}\text{Sr}/^{86}\text{Sr}$  variations  
1048 in minerals and groundmass from basalts using LA-MC-ICPMS. *Chem. Geol.*  
1049 **211**, 135–158.
- 1050 Robie R. A. and Hemingway B. S. (1995) *Thermodynamic properties of minerals*  
1051 *and related substances at 298.15 K and 1 bar ( $10^5$  Pascals) pressure and at*  
1052 *higher temperatures*. U.S. Geological Survey Bulletin 2131.
- 1053 Sachan H. K., Mukherjee B. K. and Bodnar R. J. (2007) Preservation of methane  
1054 generated during serpentinization of upper mantle rocks: Evidence from fluid  
1055 inclusions in the Nidar ophiolite, Indus Suture Zone, Ladakh (India). *Earth*  
1056 *Planet. Sci. Lett.* **257**, 47–59.
- 1057 Scambelluri M., Müntener O., Ottolini L., Pettke T. T. and Vannucci R. (2004)  
1058 The fate of B, Cl and Li in the subducted oceanic mantle and in the antigorite  
1059 breakdown fluids. *Earth Planet. Sci. Lett.* **222**, 217–234.
- 1060 Scambelluri M., Bebout G. E., Belmonte D., Gilio M., Campomenosi N., Collins  
1061 N. and Crispini L. (2016) Carbonation of subduction-zone serpentinite (high-  
1062 pressure ophi carbonate; Ligurian Western Alps) and implications for the deep  
1063 carbon cycling. *Earth Planet. Sci. Lett.* **441**, 155–166.
- 1064 Schwarzenbach E. M., Früh-Green G. L., Bernasconi S. M., Alt J. C. and Plas A.  
1065 (2013) Serpentinization and carbon sequestration: A study of two ancient  
1066 peridotite-hosted hydrothermal systems. *Chem. Geol.* **351**, 115–133.
- 1067 Scicchitano M. R., Rubatto D., Hermann J., Shen T., Padrón-Navarta J. A.,  
1068 Williams I. S. and Zheng Y.-F. (2018) *In situ* oxygen isotope determination  
1069 in serpentine minerals by ion microprobe: reference materials and applications  
1070 to ultrahigh-pressure serpentinites. *Geostand. Geoanal. Res.* **42**, 459–479.

- 1071 Sharma A., Cody G. D. and Hemley R. J. (2009) *In situ* diamond-anvil cell  
1072 observations of methanogenesis at high pressures and temperatures. *Energ.*  
1073 *Fuel.* **23**, 5571–5579.
- 1074 Sheik C. S., Cleaves II H. J., Johnson-Finn K., Giovannelli D., Kieft T. L.,  
1075 Papineau D., Schrenk M. O. and Tumiati S. (2020) Abiotic and biotic  
1076 processes that drive carboxylation and decarboxylation reactions. *Am.*  
1077 *Mineral.* **105**, 609–615.
- 1078 Shen T., Zhang L. and Li X. (2012) Geochemical characteristics of rodingite  
1079 derived from eclogite in western Tianshan, Xinjiang, China and its  
1080 implications for subduction zone fluid. *Acta Petrol. Sin.* **28**, 2235–2249.
- 1081 Shen T., Hermann J., Zhang L., Lü Z., Padrón-Navarta J. A., Xia B. and Bader T.  
1082 (2015) UHP metamorphism documented in Ti-chondrodite- and Ti-  
1083 clinohumite-bearing serpentinitized ultramafic rocks from Chinese  
1084 southwestern Tianshan. *J. Petrol.* **56**, 1425–1458.
- 1085 Shen T., Wu F., Zhang L., Hermann J., Li X. and Du J. (2016) In-situ U–Pb dating  
1086 and Nd isotopic analysis of perovskite from a rodingite blackwall associated  
1087 with UHP serpentinite from southwestern Tianshan, China. *Chem. Geol.* **431**,  
1088 67–82.
- 1089 Shi G. U., Tropper P., Cui W., Tan J. and Wang C. (2005) Methane (CH<sub>4</sub>)-bearing  
1090 fluid inclusions in the Myanmar jadeitite. *Geochem. J.* **39**, 503–516.
- 1091 Sieber M. J., Hermann J. and Yaxley G. M. (2018) An experimental investigation  
1092 of C–O–H fluid-driven carbonation of serpentinites under forearc conditions.  
1093 *Earth Planet. Sci. Lett.* **496**, 178–188.
- 1094 Sieber M. J., Yaxley G. M. and Hermann J. (2020) Investigation of fluid-driven  
1095 carbonation of a hydrated, forearc mantle wedge using serpentinite cores in  
1096 high-pressure experiments. *J. Petrol.* **61**, ega035.
- 1097 Song S., Su L., Niu Y., Lai Y. and Zhang L. (2009) CH<sub>4</sub> inclusions in orogenic  
1098 harzburgite: Evidence for reduced slab fluids and implication for redox  
1099 melting in mantle wedge. *Geochim. Cosmochim. Acta* **73**, 1737–1754.

- 1100 Steele-MacInnis M., Lecumberri-Sanchez P. and Bodnar R. J. (2012)  
1101 HOKIEFLINCS\_H<sub>2</sub>O-NaCl: A Microsoft Excel spreadsheet for interpreting  
1102 microthermometric data from fluid inclusions based on the *PVTX* properties  
1103 of H<sub>2</sub>O–NaCl. *Comput. Geosci.* **49**, 334–337.
- 1104 Syracuse E. M., van Keken P. E. and Abers G. A. (2010) The global range of  
1105 subduction zone thermal models. *Phys. Earth Planet. In.* **183**, 73–90.
- 1106 Tan Z., Agard P., Gao J., John T., Li J., Jiang T., Bayet L., Wang X. and Zhang  
1107 X. (2017) P–T–time–isotopic evolution of coesite-bearing eclogites:  
1108 Implications for exhumation processes in SW Tianshan. *Lithos* **278–281**, 1–  
1109 25.
- 1110 Tao R., Zhang L., Fei Y. and Liu Q. (2014) The effect of Fe on the stability of  
1111 dolomite at high pressure: Experimental study and petrological observation in  
1112 eclogite from southwestern Tianshan, China. *Geochim. Cosmochim. Acta* **143**,  
1113 253–267.
- 1114 Tao R., Zhang L., Tian M., Zhu J., Liu X., Liu J., Höfer H. E., Stagno V. and Fei  
1115 Y. (2018a) Formation of abiotic hydrocarbon from reduction of carbonate in  
1116 subduction zones: Constraints from petrological observation and experimental  
1117 simulation. *Geochim. Cosmochim. Acta* **239**, 390–408.
- 1118 Tao R., Zhang L., Li S., Zhu J. and Ke S. (2018b) Significant contrast in the Mg-  
1119 C-O isotopes of carbonate between carbonated eclogite and marble from the  
1120 S.W. Tianshan UHP subduction zone: Evidence for two sources of recycled  
1121 carbon. *Chem. Geol.* **483**, 65–77.
- 1122 Tian Z. L. and Wei C. J. (2013) Metamorphism of ultrahigh-pressure eclogites  
1123 from the Kebuerte Valley, South Tianshan, NW China: phase equilibria and  
1124 *P–T* path. *J. Metamorph. Geol.* **31**, 281–300.
- 1125 Truche L., McCollom T. M. and Martinez I. (2020) Hydrogen and abiotic  
1126 hydrocarbons: Molecules that change the world. *Elements* **16**, 13–18.



- 1127 Tumiati S. and Malaspina N. (2019) Redox processes and the role of carbon-  
1128 bearing volatiles from the slab–mantle interface to the mantle wedge. *J. Geol.*  
1129 *Soc.* **176**, 388–397.
- 1130 Tumiati S., Fumagalli P., Tiraboschi C. and Poli S. (2013) An experimental study  
1131 on COH-bearing peridotite up to 3.2 GPa and implications for crust–mantle  
1132 recycling. *J. Petrol.* **54**, 453–479.
- 1133 Tumiati S., Tiraboschi C., Sverjensky D. A., Pettke T., Recchia S., Ulmer P.,  
1134 Miozzi F. and Poli S. (2017) Silicate dissolution boosts the CO<sub>2</sub>  
1135 concentrations in subduction fluids. *Nat. Commun.* **8**, 616.
- 1136 Tumiati S., Tiraboschi C., Miozzi F., Vitale-Brovarone A., Manning C. E.,  
1137 Sverjensky D. A., Milani S. and Poli S. (2020) Dissolution susceptibility of  
1138 glass-like carbon versus crystalline graphite in high-pressure aqueous fluids  
1139 and implications for the behavior of organic matter in subduction zones.  
1140 *Geochim. Cosmochim. Acta* **273**, 383–402.
- 1141 Ueno Y., Yamada K., Yoshida N., Maruyama S. and Isozaki Y. (2006) Evidence  
1142 from fluid inclusions for microbial methanogenesis in the early Archaean era.  
1143 *Nature* **440**, 516–519.
- 1144 van der Straaten F., Halama R., John T., Schenk V., Hauff F. and Andersen N.  
1145 (2012) Tracing the effects of high-pressure metasomatic fluids and seawater  
1146 alteration in blueschist-facies overprinted eclogites: Implications for  
1147 subduction channel processes. *Chem. Geol.* **292–293**, 69–87.
- 1148 Veizer J., Ala D., Azmy K., Bruckschen P., Buhl D., Bruhn F., Carden G. A. F.,  
1149 Diener A., Ebner S., Godderis Y., Jasper T., Korte C., Pawellek, F., Podlaha  
1150 O. G. and Strauss H. (1999) <sup>87</sup>Sr/<sup>86</sup>Sr, δ<sup>13</sup>C and δ<sup>18</sup>O evolution of Phanerozoic  
1151 seawater. *Chem. Geol.* **161**, 59–88.
- 1152 Vitale Brovarone A., Martinez I., Elmaleh A., Compagnoni R., Chaduteau C.,  
1153 Ferraris C. and Esteve I. (2017) Massive production of abiotic methane during  
1154 subduction evidenced in metamorphosed ophicarbonates from the Italian Alps.  
1155 *Nat. Commun.* **8**, 14134.

- 1156 Vitale Brovarone A., Sverjensky D. A., Piccoli F., Ressico F., Giovannelli D. and  
1157 Daniel I. (2020) Subduction hides high-pressure sources of energy that may  
1158 feed the deep subsurface biosphere. *Nat. Commun.* **11**, 3880.
- 1159 Vroon P. Z., van der Wagt B., Koornneef J. M. and Davies G. R. (2008) Problems  
1160 in obtaining precise and accurate Sr isotope analysis from geological materials  
1161 using laser ablation MC-ICPMS. *Anal. Bioanal. Chem.* **390**, 465–476.
- 1162 Wheat C. G., Seewald J. S. and Takai K. (2020) Fluid transport and reaction  
1163 processes within a serpentinite mud volcano: South Chamorro Seamount.  
1164 *Geochim. Cosmochim. Acta* **269**, 413–428.
- 1165 Whitney D. L. and Evans B. W. (2010) Abbreviations for names of rock-forming  
1166 minerals. *Am. Mineral.* **95**, 185–187.
- 1167 Woodhead J., Swearer S., Hergt J. and Maas R. (2005) *In situ* Sr-isotope analysis  
1168 of carbonates by LA-MC-ICP-MS: interference corrections, high spatial  
1169 resolution and an example from otolith studies. *J. Anal. At. Spectrom.* **20**, 22–  
1170 27.
- 1171 Xia B., Zhang L., Xia Y. and Bader T. (2014) The tectonic evolution of the  
1172 Tianshan Orogenic Belt: Evidence from U–Pb dating of detrital zircons from  
1173 the Chinese southwestern Tianshan accretionary mélange. *Gondwana Res.* **25**,  
1174 1627–1643.
- 1175 Xu H., Zhao Y., Vogel S. C., Daemen L. L. and Hickmott D. D. (2007)  
1176 Anisotropic thermal expansion and hydrogen bonding behavior of portlandite:  
1177 A high-temperature neutron diffraction study. *J. Solid State Chem.* **180**, 1519–  
1178 1525.
- 1179 Yang Y., Wu F., Xie L., Yang J. and Zhang Y. (2009) In-situ Sr isotopic  
1180 measurement of natural geological samples by LA-MC-ICP-MS. *Acta Petrol.*  
1181 *Sin.* **25**, 3431–3441.
- 1182 Yang C., Ni Z., Wang T., Chen Z., Hong H., Wen L., Luo B. and Wang W. (2018)  
1183 A new genetic mechanism of natural gas accumulation. *Sci. Rep.* **8**, 8336.

- 1184 Zhang L., Du J., Lü Z., Yang X., Gou L., Xia B., Chen Z., Wei C. and Song S.  
1185 (2013) A huge oceanic-type UHP metamorphic belt in southwestern Tianshan,  
1186 China: Peak metamorphic age and  $P$ – $T$  path. *Chinese Sci. Bull.* **58**, 4378–4383.
- 1187 Zhang L., Wang Y., Zhang L. and Lü Z. (2019) Ultrahigh pressure metamorphism  
1188 and tectonic evolution of southwestern Tianshan orogenic belt, China: a  
1189 comprehensive review. In *HP–UHP Metamorphism and Tectonic Evolution*  
1190 *of Orogenic Belts* (eds. L. Zhang, Z. Zhang, H.-P. Schertl and C. Wei).  
1191 Geological Society, London, Special Publications. pp. 133–152.
- 1192 Zhang L., Wang Q., Ding X. and Li W.-C. (2021) Diverse serpentinization and  
1193 associated abiotic methanogenesis within multiple types of olivine-hosted  
1194 fluid inclusions in orogenic peridotite from northern Tibet. *Geochim.*  
1195 *Cosmochim. Acta* **296**, 1–17.
- 1196 Zhu J., Zhang L., Lü Z. and Bader T. (2018) Elemental and isotopic (C, O, Sr, Nd)  
1197 compositions of Late Paleozoic carbonated eclogite and marble from the SW  
1198 Tianshan UHP belt, NW China: Implications for deep carbon cycle. *J. Asian*  
1199 *Earth Sci.* **153**, 307–324.
- 1200 Zhu J., Zhang L., Tao R. and Fei Y. (2020) The formation of graphite-rich eclogite  
1201 vein in S.W. Tianshan (China) and its implication for deep carbon cycling in  
1202 subduction zone. *Chem. Geol.* **533**, 119430.

1203

## 1204 **FIGURE CAPTIONS**

1205 **Fig. 1.** Geological background of the Chinese southwestern Tianshan. (A)  
1206 Simplified tectonic framework of the western part of the Chinese Tianshan  
1207 (modified from [Tian and Wei, 2013](#)). (B) Schematic geological map of the  
1208 Chinese southwestern Tianshan HP–UHP metamorphic belt (modified from  
1209 [Zhang et al., 2013](#)). Grey stars show sample localities of CH<sub>4</sub>-bearing carbonated  
1210 eclogites at Kebuerte and Habutengsu in the metamorphic belt ([Tao et al., 2018a](#)).  
1211 (C) Detailed geological map of Changawuzi showing the sample locality of CH<sub>4</sub>-  
1212 bearing ophidolomites in this study (modified from [Shen et al., 2015](#)).

1213

1214 **Fig. 2.** Petrological characteristics of the studied ophidolomites. (A and B)  
1215 Discontinuous and folded dolomite veins (with the rim encircled by yellowish  
1216 calcite and brucite) filling the host serpentinites (hand-specimen scale). (C and D)  
1217 Dolomite growth at the expense of antigorite, with unreacted antigorite visible  
1218 (cross-polarized light). In some cases, antigorite shows abnormal interference  
1219 colors due to the thick sections. (E and F) Decomposition of dolomite into cloudy  
1220 calcite and brucite (cross-polarized light). (G) Back-scattered electron image (the  
1221 upper part) and compositional X-ray map (the lower part) of dolomite  
1222 decomposition into calcite–brucite intergrowths. The newly grown calcite and  
1223 brucite extend into the inner parts of dolomite along microcracks. (H) The  
1224 enlargement of the box in (G) showing intergrowths of acicular calcite and brucite  
1225 and patches of relict dolomite in calcite. Mineral abbreviations in this study follow  
1226 [Whitney and Evans \(2010\)](#).

1227

1228 **Fig. 3.** Occurrence of olivine and microstructures of magnetite-hosted mineral  
1229 inclusions in the studied ophidolomites. (A) Olivine relicts in the antigorite matrix.  
1230 (B) Coarse magnetite grains enclosing abundant minerals in the matrix of  
1231 antigorite and dolomite. (C) Olivine in association with antigorite and brucite in  
1232 magnetite. (D) Calcite and brucite growth at the expense of dolomite in magnetite,  
1233 with dolomite relicts visible.

1234

1235 **Fig. 4.** Petrographic characteristics of fluid inclusions in the studied  
1236 ophidolomites. (A and B) Type-I two-phase (vapor and liquid) fluid inclusions in  
1237 dolomite. (C and D) Type-II single-phase fluid inclusions in dolomite. (E–G)  
1238 Type-I two-phase (vapor and liquid) fluid inclusions in calcite intergrown with  
1239 brucite.

1240

1241 **Fig. 5.** Raman spectra of fluid inclusions in the studied ophidolomites. (A and B)  
1242 Type-I CH<sub>4</sub>-bearing aqueous fluid inclusions in dolomite (A) and calcite  
1243 intergrown with brucite (B). The strong fluorescence of the host carbonates  
1244 sometimes prevents conclusive Raman investigation of the liquid phase of H<sub>2</sub>O.  
1245 (C) Type-II CH<sub>4</sub> ± H<sub>2</sub>-bearing fluid inclusions in dolomite. Weaker but crucial  
1246 peaks are enlarged. Scale bars of the close-up images are 10 μm.

1247

1248 **Fig. 6.** Isotope compositions of the studied ophidolomites. (A) *In situ* Sr isotope  
1249 compositions of dolomite and calcite. The sky blue and purple dashed lines show  
1250 <sup>87</sup>Sr/<sup>86</sup>Sr ratios of the Tianshan HP ophidolomites and their dolomite separates  
1251 (Peng et al., 2020) and the Ordovician–Carboniferous seawater (Veizer et al.,  
1252 1999), respectively. The Tianshan UHP serpentinites are marine-originated (Shen  
1253 et al., 2015) and have largely inherited Sr isotope compositions of the seawater  
1254 (Peng et al., 2020). The sky blue and purple solid lines show the average <sup>87</sup>Sr/<sup>86</sup>Sr  
1255 ratios of dolomite and calcite, respectively. Error bars represent the 2σ internal  
1256 precision. (B) C and O isotope compositions of dolomite and calcite. For  
1257 comparison, δ<sup>13</sup>C and δ<sup>18</sup>O of carbonates in various lithologies from the Chinese  
1258 southwestern Tianshan are plotted (van der Straaten et al., 2012; Collins et al.,  
1259 2015; Peng et al., 2018, 2020; Zhu et al., 2018). The green and grey areas display  
1260 δ<sup>13</sup>C of marine carbonates (Hoefs, 2009) and carbonates in CH<sub>4</sub>-bearing  
1261 ophicalcites from the Western Alps (Vitale Brovarone et al., 2017), respectively.  
1262 The black and blue solid lines correspond to C isotopic trends of carbonates  
1263 affected by decarbonation and carbonate reduction from Galvez et al. (2013b),  
1264 while the black and blue dashed lines represent the possible trends of  
1265 decarbonation and carbonate reduction in the Tianshan. Uncertainties of values  
1266 are smaller than the symbol sizes.

1267

1268 **Fig. 7.** (A) Stabilities of phases under variable *f*O<sub>2</sub>–*f*H<sub>2</sub> conditions in the Ca–Mg–  
1269 C–O–H system (with fixed Ca:Mg:C of 1:1:2 in molar ratio) at 8 kbar and 420 °C.

1270 The orange dashed lines show  $\log f\text{O}_2$  of magnetite–hematite (MH), fayalite–  
1271 magnetite–quartz (FMQ), and iron–magnetite (IM) buffers calculated at 8 kbar  
1272 and 420 °C. The pink solid line represents the thermodynamically calculated  
1273 model of slightly reduced  $\text{H}_2\text{O}$  at  $X_{\text{O}} = 0.33 \sim 1/3$  in the H–O system (star:  $X_{\text{O}} =$   
1274  $0.33333323$ , corresponding to  $y_{\text{H}_2\text{O}} = 0.999995$  and  $y_{\text{H}_2} = 0.000005$ ). (B) The  $P$ – $T$   
1275 pseudosection displaying diverse phase assemblages in the Ca–Fe–Mg–Si–C–O–  
1276 H system at  $\log f\text{O}_2 = -26.0$  and  $\log f\text{H}_2 = 0.8$ . The rectangle confines  $P$ – $T$   
1277 conditions for the onset of retrograde serpentinization in the Tianshan (7–9 kbar  
1278 and 410–430 °C; [Li et al., 2007, 2010](#)).

1279

1280 **Fig. 8.**  $P$ – $T$  diagram showing stages of dolomite reduction and fluid entrapment  
1281 during exhumation of the Chinese southwestern Tianshan. Stage A represents the  
1282 onset of dolomite reduction, inferred from retrograde serpentinization starting at  
1283 7–9 kbar and 410–430 °C and propagating to lower  $P$ – $T$  conditions (Stage B) in  
1284 the Tianshan ([Li et al., 2007, 2010](#)). Solid lines marked with 1, 2, and 3 display  
1285 the controversial  $P$ – $T$  conditions for the chrysotile to antigorite transition from [Li](#)  
1286 [et al. \(2007, 2010\)](#), [Scambelluri et al. \(2004\)](#), and [Evans et al. \(1976\)](#), respectively,  
1287 resulting in uncertainties of Stage B. The constrained  $P$ – $T$  conditions for fluid  
1288 entrapment (Stage C) are based on the fluid inclusion isochores intersecting the  
1289 retrograde  $P$ – $T$  path of the Tianshan ([Tan et al., 2017](#)). The stability fields of  
1290 lizardite, antigorite, and olivine, as well as the main transformation reactions and  
1291 cold subduction gradient, are from [Guillot et al. \(2015\)](#). The calcite to aragonite  
1292 transition is from [Johannes and Puhan \(1971\)](#).

1293

1294 **Fig. 9.** (A) Summary of abiotic  $\text{CH}_4$  formation through dolomite reduction in  
1295 ophidolomites during exhumation of the Chinese southwestern Tianshan. The  $P$ –  
1296  $T$  constraints for HP ophidolomites in the Tianshan are from [Peng et al. \(2020\)](#).  
1297 The red rectangle [T] displays  $P$ – $T$  conditions for the onset of dolomite reduction,  
1298 inferred from retrograde serpentinization in the Tianshan ([Li et al., 2007, 2010](#)).

1299 For comparison,  $P$ – $T$  estimates for carbonate reduction during shallow subduction  
1300 in Alpine Corsica [C] ([Malvoison et al., 2012](#); [Galvez et al., 2013a, b](#)) and the  
1301 Italian Alps [A] ([Vitale Brovarone et al., 2017](#); [Giuntoli et al., 2020](#)) are shown.  
1302 The  $P$ – $T$  path of the Tianshan is from [Tan et al. \(2017\)](#). The cyan and light cyan  
1303 areas represent the modelled prograde  $P$ – $T$  paths of subduction zones at the slab  
1304 interface and slab Moho (7 km beneath the slab surface; [Syracuse et al., 2010](#)),  
1305 respectively. The sky blue solid curve (PD) shows the global average range of  
1306 prograde  $P$ – $T$  paths from subduction-related metamorphic rocks ([Penniston-  
1307 Dorland et al., 2015](#)). Facies boundaries and abbreviations are from [Liou et al.  
1308 \(2004\)](#). (B) General model showing abiotic  $\text{CH}_4$  production through dolomite  
1309 reduction during shallow subduction. Due to uncertainties in the scale and extent  
1310 of serpentinization in subducted slabs ([Li et al., 2007, 2010](#); [Vitale Brovarone et  
1311 al., 2017, 2020](#); [Lazar, 2020](#)), dashed arrow lines represent fluid migration  
1312 pathways instead of the steady fluid flow. The extent of alteration is dependent on  
1313 the infiltration of the reactive reduced fluids. Possible  $\text{CH}_4$ – $\text{H}_2$ -generating  
1314 reactions are listed but without stoichiometric numbers. Figure is not to scale.